THE PENNSYLVANIA STATE UNIVERSITY
SCHREYER HONORS COLLEGE

BROWNIAN DYNAMICS SIMULATION OF KINESIN MOTOR PROTEIN DYNAMICS

ANNAN S. I. COOK
SPRING 2019

A thesis
submitted in partial fulfillment
of the requirements
for a baccalaureate degree
in Physics
with honors in Biomedical Engineering

Reviewed and approved* by the following:

William O. Hancock
Professor of Biomedical Engineering
Thesis Supervisor

William O. Hancock
Professor of Biomedical Engineering
Honors Adviser

Justin Brown
Professor of Biomedical Engineering
Committee Member
* Signatures are on file in the Schreyer Honors College.

ABSTRACT

High frequency nanoparticle tracking has emerged in recent years as a powerful strategy to track the nanoscale dynamics of proteins, DNA, and other biomolecules. Using dark-field or interferometric scattering microscopy techniques (iScat) in conjunction with point-spread fitting, sub-millisecond temporal resolution images of nanoparticle-labeled proteins can be achieved with nanometer spatial precision. However, there remain unresolved questions regarding the best practices for site-specific tagging of proteins. In this thesis, Brownian dynamics simulations and artificial image generation techniques are employed to investigate the influence of tether length, tether stiffness, and particle size on imaging precision and the ability to accurately measure protein fluctuation dynamics. The first finding is that point spread function fitting cannot be extended to arbitrarily fast frame rates because the gold probe undergoes tethered diffusion about its anchor point. One implication is that camera exposure times that allow the probe to fully explore its positional distribution increase fitting precision. The second finding is that changes in protein rotational freedom give rise to artifactual translations of the nanoparticle position that do not necessarily correlate with actual protein dynamics. These lessons are employed to interpret experimental data of gold nanoparticle-labeled kinesin motor proteins stepping along microtubules. It is found that apparent discrepancies in the literature regarding the structure of the kinesin dimer in the ATP waiting state are due to the differences in label strategy and gold attachment position. These results emphasize the importance of carefully considering controllable conjugation and imaging parameters when designing and interpreting gold nanoparticle tracking experiments and provide new insights into the protein dynamics underlying the kinesin mechanochemical cycle.

TABLE OF CONTENTS

LIST OF FIGURES

LIST OF TABLES

ACKNOWLEDGEMENTS

Chapter 1

Introduction

1.1 Kinesin Overview

1.1.1 Kinesin motors facilitate transport processes in the cell

The organized transport of cell materials is vital to the healthy function and survival of eukaryotic cells. mRNA and newly synthesized protein molecules are transported along the cytoskeletal filaments of the cell in a chaotic dance of vesicles and protein assemblies to facilitate the metabolic processes that give rise to complex life. In order to maintain this intricate organization, three main superfamilies of molecular motor proteins have evolved to exploit the underlying cytoskeletal architecture of eukaryotic cells. These motor proteins include myosin, which function by interacting with the actin cytoskeleton, and dynein and kinesin motors, which use the microtubule cytoskeleton as a sort of freight rail to transport cell materials. The subject of this work, kinesin, is encoded by 45 mammalian kinesin superfamily (KIF) genes that constitute 14 families(1). As their diverse classification suggests, kinesins are responsible for varied and numerous vital processes in the body, including the regulation of microtubule dynamics during mitosis and the organization of the mitotic spindle, fast axonal transport in neurons, and trafficking mRNA and vesicle-bound proteins(1).

Kinesins specialized for transport, like kinesin-1, bind vesicles, organelles, and proteins and localize them in neuronal structures. Typically, kinesins work in assemblies of multiple motor types including both anterograde (plus-end directed) kinesin motors which transport cargoes to the cell periphery, and retrograde (minus-end directed) motors, like dynein, which transport cargoes toward the cell soma. In this process, dynein and kinesin work together to transport cargoes bidirectionally in

neurons and other cell structures(2). Understanding the dynamics of multi-motor transport, especially

with regard to their mechanisms of activation and inhibition, could be vital to understanding the nature of

neurodegenerative diseases. For instance, MAP7, and Tau are microtubule associated proteins (MAPs)

that enhance and inhibit kinesin processivity depending on their distribution in the cell(3). Pathological

function of these MAPs, wherein they form β-sheet tangles, are implicated in Alzheimer's disease(4), and

therefore understanding the role of kinesin in the formation of these tangles is an important step toward

finding a cure for that disease.
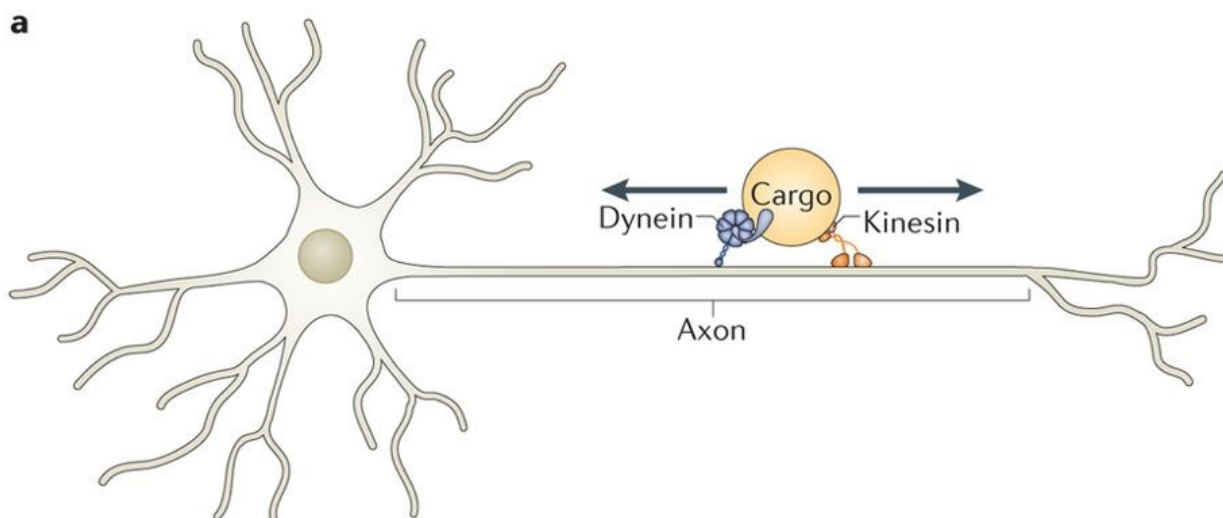
Figure 1. Bidirectional cargo transport involves many motor types. The plus-end of the microtubule is oriented toward the cell periphery, while the minus-end is oriented toward the cell body. Kinesin steps toward the periphery while dynein steps toward the cell body. Figure adapted from Hancock**(2)**

1.1.2 Kinesin is a dimeric motor protein that converts chemical energy into mechanical work

Kinesin motors are homodimeric processive enzymes that undergo cyclic structural transitions driven by ATP binding and hydrolysis to generate directed motion. The key components of the motor are depicted in Figure 2. In brief, the motor is comprised of two globular motor domains, which do the heavy lifting of binding to the microtubule, binding ATP, and catalyzing hydrolysis to drive stepping (Figure 2A). In order to associate with the multitude of intracellular cargoes, the cargo adaptor, or kinesin light chain (Figure 2C), has a variable structure depending on the cargo type, and rests at the end of a coiled-coil stalk (Figure 2B). The two motor domains are connected to the coiled-coil region via a disordered, 14 amino acid polypeptide region, called the neck-linker(5) . This neck-linker region is the mechanical element of the motor that is crucial for kinesin motility.
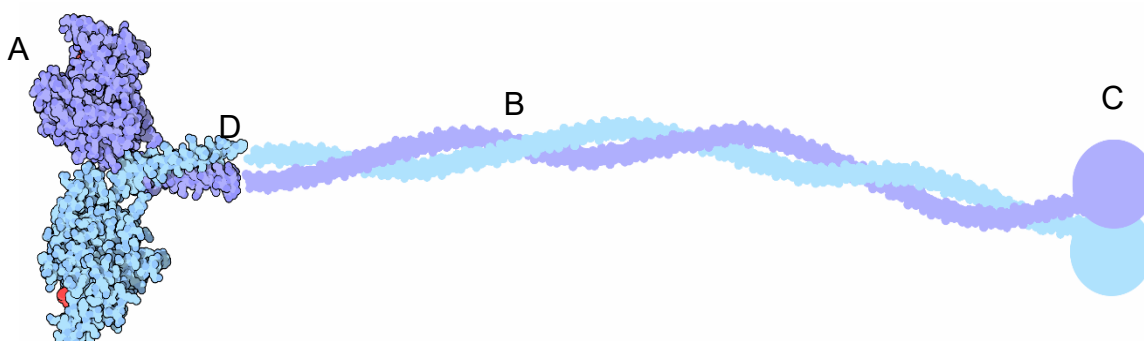
Figure 2. A conventional kinesin molecule. The (A) motor heads are responsible for binding to the microtubule and hydrolyzing ATP. The (B) coiled coil stalk acts as a tether to connect the motor heads to the (C) cargo adaptor subunit. The (D) neck-linker region couples the hydrolysis cycles of the two motor heads to conformational changes to enable processive stepping. Figure adapted from Goodsell (33).

In ATP driven stepping, kinesin walks along a single protofilament of a microtubule by taking 8.2 nm center of mass steps between tubulin subunits (6). It does so by "walking" in a hand-over-hand fashion, swinging one head in front of the other one in 16.4 nm increments. The conventional model of the kinesin mechanochemical cycle posits that the free energy of ATP binding drives a conformational change in a switch loop γ-phosphate sensor, and transmits this motion through a switch-II, or relay, α-helix which drives the neck linker from a disordered state to an alignment with a β-sheet along the motor

domain of the leading head(5) . The kinesin head thereby biases the tethered diffusion of the motor head

to the next tubulin dimer, permitting binding and completion of the step.
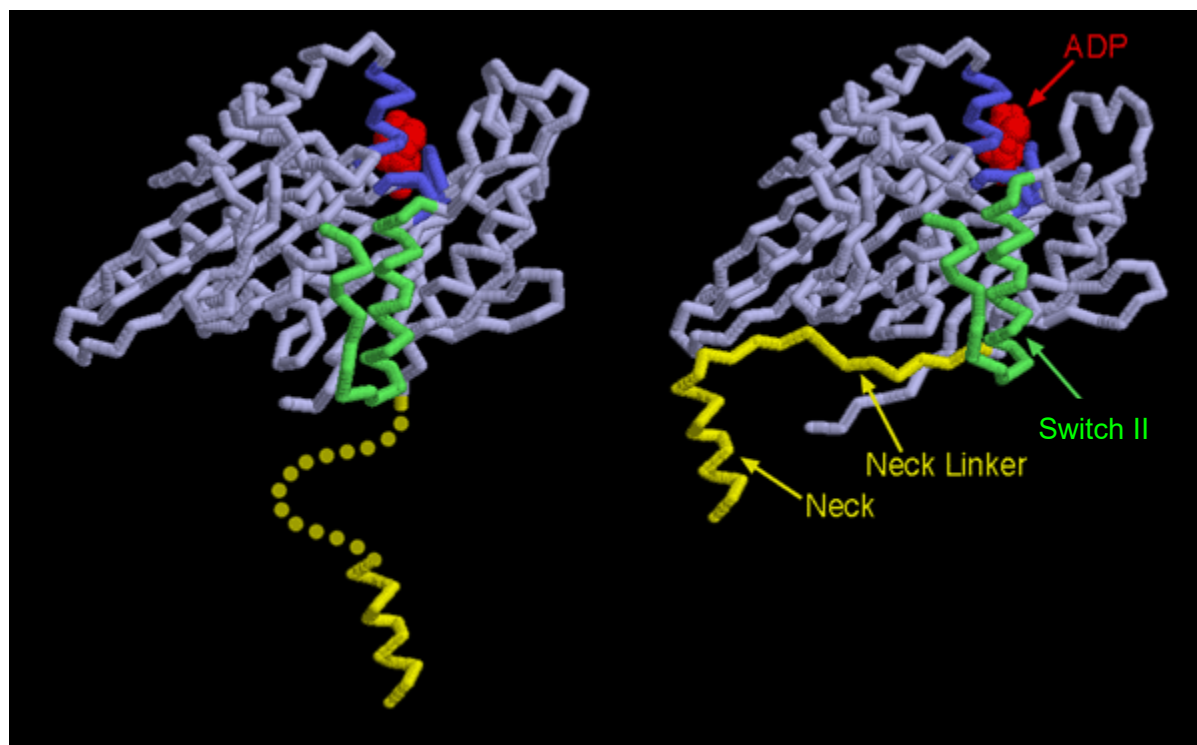
Figure 3. Depiction of the disordered (left) to ordered (right) transition of the neck linker region. The binding of ATP induces structural changes local to the binding pocket of the motor head, that are then communicated to the neck linker region by the so-called relay helix. The alignment of the neck linker along the front of the motor head biases the diffusion of the free head, allowing the free head to find the next tubulin subunit, and complete the step. Figure adapted from Goodsell (33).

The mechanochemical cycle of kinesin consists of several biochemical states that have been

elucidated by kinetic experiments, fluorescence microscopy, and optical trap techniques(7–9). A model

of the kinetic cycle is depicted in Figure 4. Starting with state [1] in the figure, the nucleotide-free

leading head waits for ATP to bind, while the rear, ADP bound head remains weakly associated with the

protofilament behind the leading head. As ATP binds, the neck-linker docks, swinging the trailing head

forward, depicted in [2] in the figure. The hydrolysis of ATP then occurs, fully docking the neck linker

forward and allowing the unbound head to attempt to bind to the next tubulin binding site [3]. What

occurs next is best described as a kinetic race between the release of inorganic phosphate on the bound

head [4_{off}] and the completion of the step [4]. This race appears to occur because the affinity of the heads

are phosphate dependent.(9)
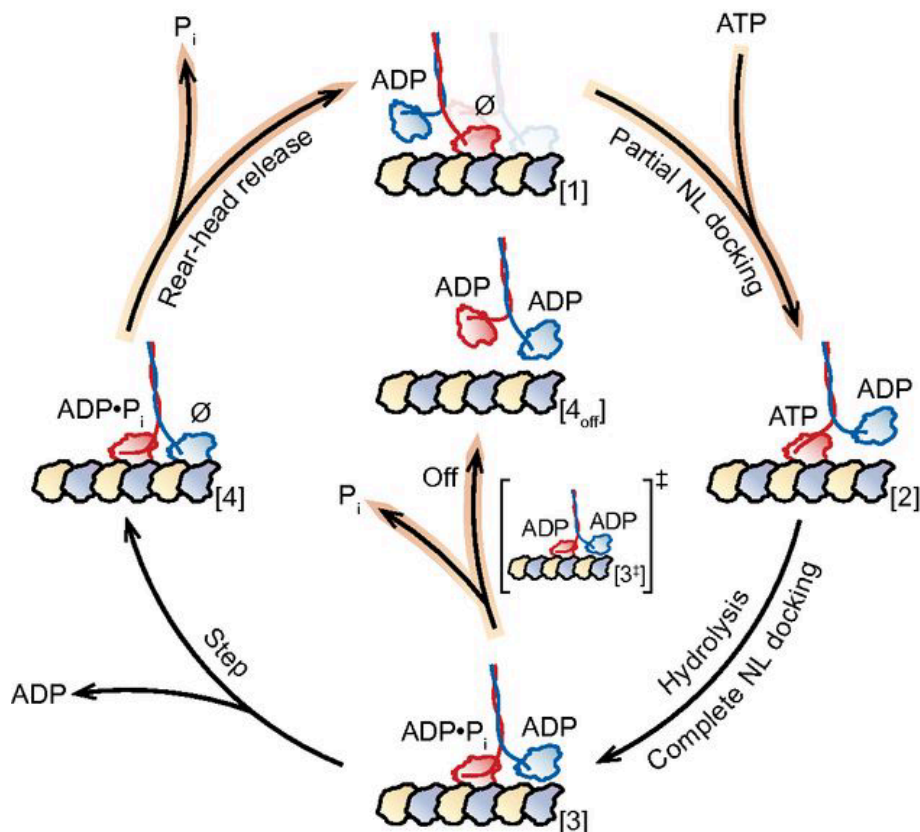
Figure 4. The hydrolysis cycle of kinesin-1. [1] The front head waits for ATP while the rear motor head sits biased to the tubulin subunit. [2] Upon ATP binding, the rear head transitions forward as the neck linker docks to the front head. [3] ATP hydrolysis completes the docking of the neck linker. [4] The free head binds to the subsequent tubulin binding location, or [4_{off}] phosphate dependent changes in affinity lead to the release of the motor from the microtubule. Figure adapted from Milic *et. al.* (9)

Kinesin steps are sufficiently rapid, and occur with such frequency (~100 s^{-1}) that optical traps

and conventional fluorescence techniques simply do not have the spatiotemporal resolution required to

resolve the short-lived intermediate states in this mechanochemical cycle. The ATP waiting state of the

motor, step [1], is a particularly difficult state to resolve using conventional methods, and at

physiologically relevant ATP concentrations. Therefore questions remain regarding its detailed structure,

both spatially and temporally(7). To answer these questions, higher framerate techniques are required to resolve the nature of the transient, ATP dependent state.

1.2 Principles of Diffraction Limited Imaging

1.2.1 Superresolution imaging of fluorophores is a powerful tool in biological imaging

In the past two decades, fluorescence imaging has undergone a renaissance due to the introduction of superresolution microscopy to the field of biology, whereby light sources much smaller than the diffraction limit of the imaging apparatus are fit to extract positional information to nanometer precision. In particular, fluorescence imaging with one nanometer accuracy (FIONA) uses a point spread function (PSF) fitting approach, whereby the Airy Disc diffraction pattern of a fluorescent label is approximated using a 2D Gaussian intensity distribution, and the mean of the distribution is assumed to correspond to the true location of the fluorophore(10). Coupling this approach with total internal reflection fluorescence microscopy (TIRFM) allows for the reduction of background radiation because the only fluorophores excited by the incident light are those within the boundaries of the evanescent field produced by the totally reflected light. Hence, by affixing microtubules to a glass coverslip and introducing motor proteins and ATP, it is possible to watch live molecular motors step, and localize their positions to within 1 nm(11). This approach has shed light on the mechanisms by which molecular motors, like kinesin, step, as Yildiz et. al. were able to resolve a standing question about whether kinesin walked via a hand over hand mechanism, or by an inchworm stepping mechanism (12).
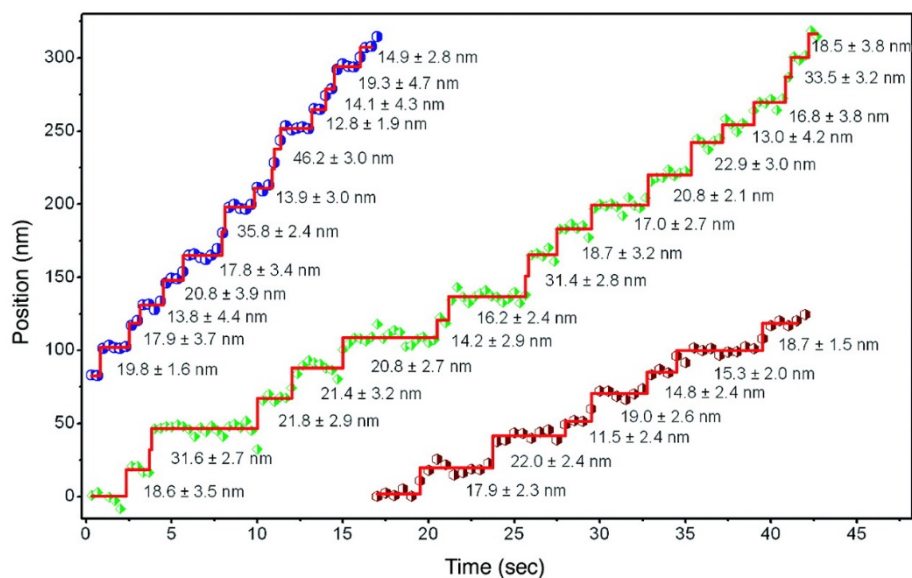
Figure 5. Yildiz et. al. were able to fit the intensity profile of a fluorescently labeled kinesin motor in order to resolve 16.4 nm steps of a single kinesin head. This observation confirmed the hand over hand model of kinesin motility. Figure adapted from Yildiz et. al. (12).

1.2.2 Photon flux limits the precision of fitting of fluorescence signals

Though superresolution techniques are broadly applicable to *in vitro* assays, the fluorescence process is temporally limited because of the nanoseconds required for a fluorophore to become excited, and return to its ground state. Indeed, the standard error of the mean position of the Gaussian distribution goes as $1/\sqrt{N}$, with N equal to the number of photons collected during an exposure window(13). For this reason, using fluorescent dyes necessitates the use of exposure times on the order of 500 milliseconds in order to collect sufficient photons to fully localize the protein and to achieve acceptable signal to noise ratios. Therefore, these assays are unable to probe the fast dynamics of kinesin motors, whose conformational changes occur on sub-millisecond timescales at physiologically relevant ATP

concentrations (7, 14, 15). In order to address these limitations, probes with higher photon fluxes are required.
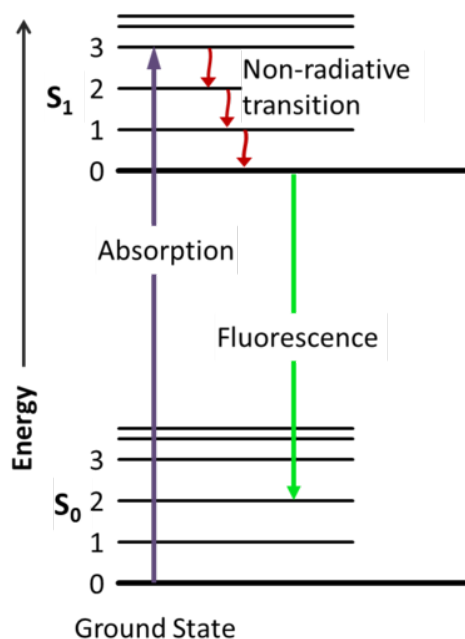
Figure 6. Because of the various events that can occur between the absorption of a photon, and the emission of a fluorescent photon, the timescale of fluorescence takes several nanoseconds

1.2.3 Gold nanoparticle labels achieve better temporal resolution than traditional fluorophores

In order to mitigate the photon flux issues of conventional fluorophores, researchers have transitioned to using gold-nanoparticle probes, which utilize light scattering instead of fluorescence to collect photons. By conjugating gold nanoparticle probes to the protein of interest, sub-millisecond temporal resolution is achievable. For example, in 2001, Yasuda *et. al.* were able to observe the rotations of the F1-ATPase labeled with a 40-nm gold nanoparticle at 8,000 frames per second, establishing that

point-spread function (PSF) fitting can be extended to extremely fast tracking regimes (16). To exploit

this gold labeling strategy, modifications to the total internal reflection set up called TIR dark-field

microscopy (TIRDFM), and interferometric scattering microscopy (iScat) could achieve 1 nm localization

at microsecond camera exposure times(7, 8, 17–19). TIRDFM again relies on an evanescent wave to

produce a scattering signal on proteins affixed near a glass surface with the subtle difference that the

background has no fluorophores and so appears black. iScat, on the other hand, uses small differences in

optical path length to achieve phase contrast in the light signal. Using this technique, one can visualize

label-free microtubules on a glass surface which can be a decided advantage when visualizing the steps of

a kinesin motor. The application of these imaging modalities has opened the door to the detection of

previously unresolvable structural transitions in motor proteins(7, 8). However, because the gold label

used in these experiments requires a tether to affix the probe to the protein, it also introduces questions

regarding the underlying dynamics of the gold probe, and to what extent these dynamics influence

experimental observations.

1.3 Standing Questions in Kinesin Single Molecule Experiments

1.3.1. Choice of label position leads to different conclusions about the structure of the ATP waiting state

A controversy regarding the dynamics of the kinesin step arose when two papers presented the

fast dynamics of kinesin, but drew opposite conclusions about the structure of the kinesin-1 ATP waiting

state (7, 8). Results reported in Mickolajczyk et. al. used iScat microscopy to observe kinesin-1 motors

functionalized with an N-Terminal Avi-Tag label connected to a 30 nm gold nanoparticle (7). This

tethering moiety emanates from the right-hand side of the microtubule bound head. The traces reported in

this paper suggest the observation of a transient 1 head bound intermediate state, but suggest a two-heads-

bound ATP waiting state, as there is no corresponding displacement of the head coincident with the

waiting state. These observations suggest a powerstroke-like stepping mechanism, wherein the trailing

head waits in a strongly bound state on the microtubule, and the binding of ATP is sufficient to break the

interaction of the bound head and microtubule. Furthermore, as the

kinesin steps, the traces show essentially no rightward displacement of the head as it walks.
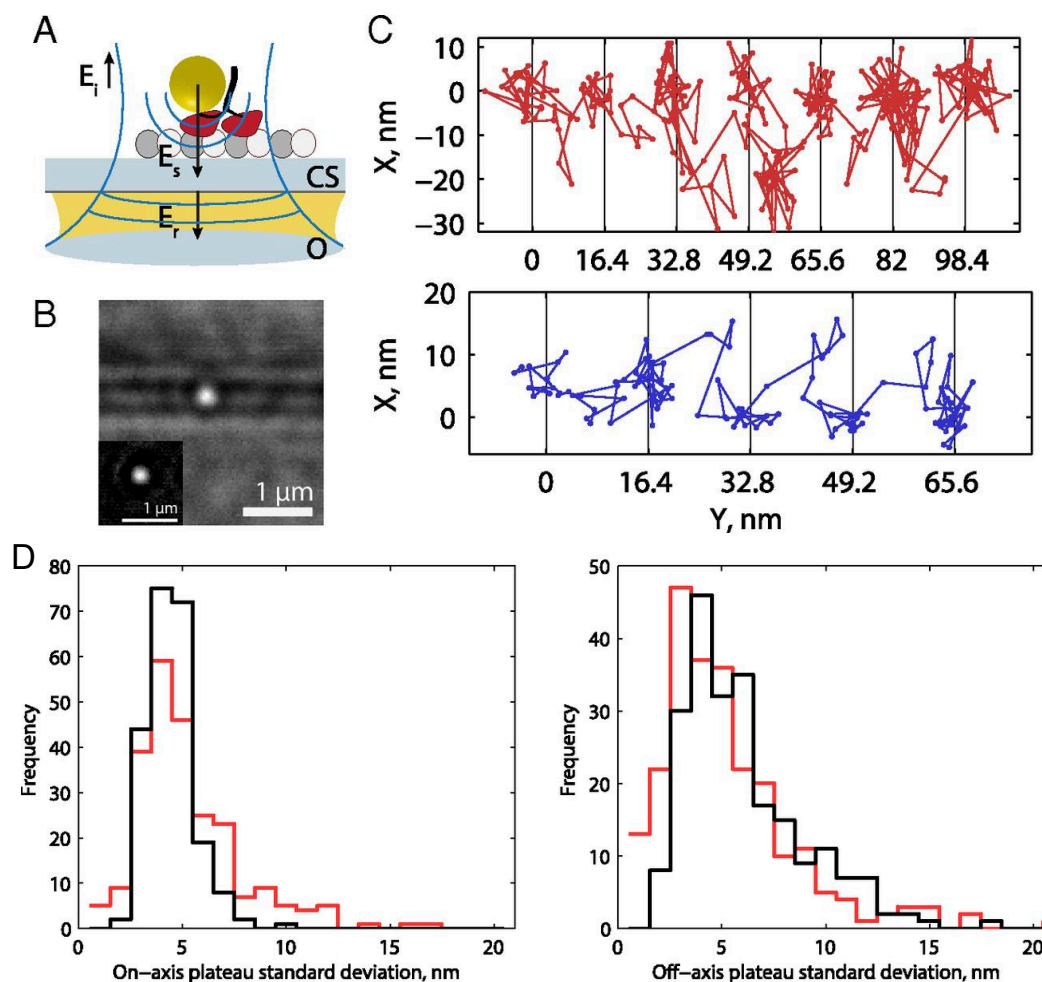
Figure 7. (A) The experimental set up of iScat microscopy experiments conducted in Mickolajczyk *et. al.* (B) Sample iScat image depicting the label free contrast of the microtubules, and a gold nanoparticle resting on the microtubule surface. The inset shows the same image with the background subtracted. (C) Typical traces displaying 16.2 nm displacements per step. The images were fitted using PSF fitting algorithms. (D) Illustration of the relatively small (~5 nm) off axis displacement of the signal. Figure adapted from Mickolajczyk *et. al.* (7).

These conclusions contrast with those results reported in Isojima et. al. Here, the experimenters used TIR Dark field single molecule assays of a kinesin-1 motor fused to a biotin-PEG2-maleimide tag at mutations to the S55 and E215 locations with a cysteine residue. The cysteine residue was then conjugated to a streptavidin-coated, 40 nm gold nanoparticle(8). The traces reported in this paper suggest the existence of a longer lived one-head-bound state, where the labeled head transitions to the right hand side of the microtubule. These results are consistent with a 1 head bound ATP waiting state. Puzzlingly, the rightward transitions observed in this paper correlate with two different displacements along the microtubule. In the S55 case, the rightward transition is accompanied by a forward displacement of the motor as it waits for ATP. In contrast, the E215 construct displaces rightward and backward.
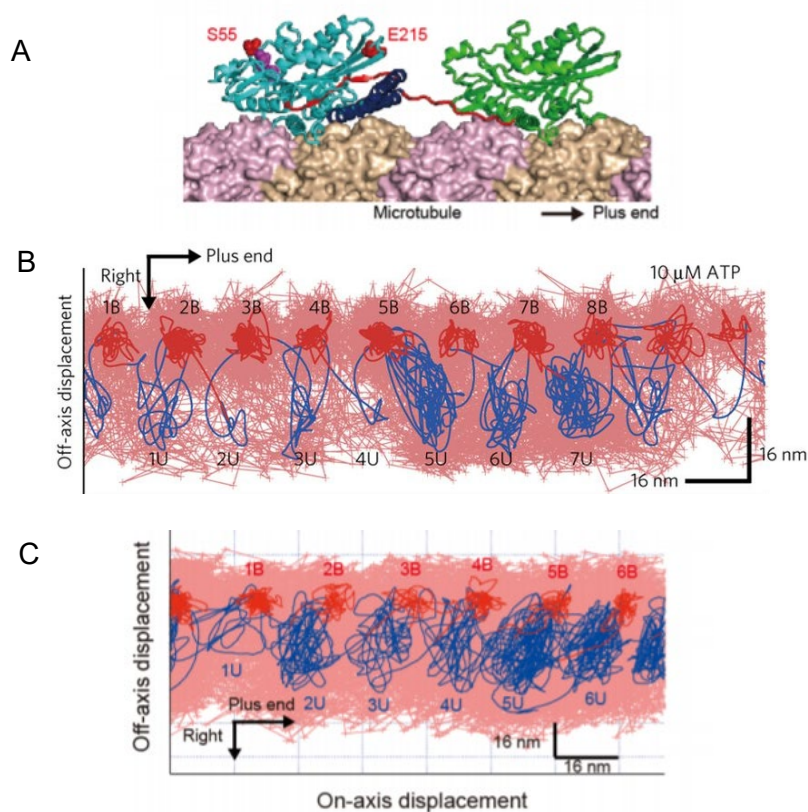
Figure 8. The use of different label positions, including the S55 and E215 (A) positions on the kinesin head can lead to different characteristic stepping patterns. The (B) S55 label position shows a clear righward and forward displacement in the ATP waiting state, while the (C) E215 label positions shows a clear righward and backward displacement in the ATP waiting state. Figure adapted from Isojima *et. al.* (8).

1.3.2 Brownian Dynamics simulations can probe questions pertaining to the limitations of gold tracking, and about the underlying dynamics of labeled kinesin motors

In the present work, Brownian Dynamics models of the diffusion of nanoparticles are used to generate imaging data, and to use this imaging data to address questions pertaining to experimental parameters used in gold labeling experiments using kinesin molecular motors. Specifically, these simulations will address the influence of controllable experimental parameters including nanoparticle size, nanoparticle tether properties, exposure time, and photon flux on the RMS error of the fitted image data. From there, the lessons learned are applied to generalized protein conformational changes. Finally, the lessons gleaned from simplified models are applied to kinesin stepping. It is found that label position has a strong influence on the observed stepping patterns, and that apparent discrepancies in kinesin stepping are due to the choice of tether moiety and label position. It is found that the ATP waiting state of kinesin is, in fact, a weakly associated, rightward displaced structural state that is undisplaced longitudinally from the previous binding location. These results underscore the importance of considering the dynamics of the probe and the influence of label position on experimental observations, and the fact that overinterpreting results can lead to erroneous conclusions.

Chapter 2

Methods

2.1 Computational Overview

In order to simulate the overdamped motion of the kinesin-1 and the gold nanoparticle probe, a numerical implementation of the overdamped Langevin Equation was employed. The dynamics of the kinesin head and nanoparticle were integrated for 1 ms, and images were generated based on the position of the nanoparticle. With the images generated, the intensity profiles were fit using a point spread fitting software. The relevant statistics and data were computed from the fits to the images.

A

hν   hν

1. Simulate Dynamics   2. Generate Photons   3. Create Image   4. Fit PSF to Image Data
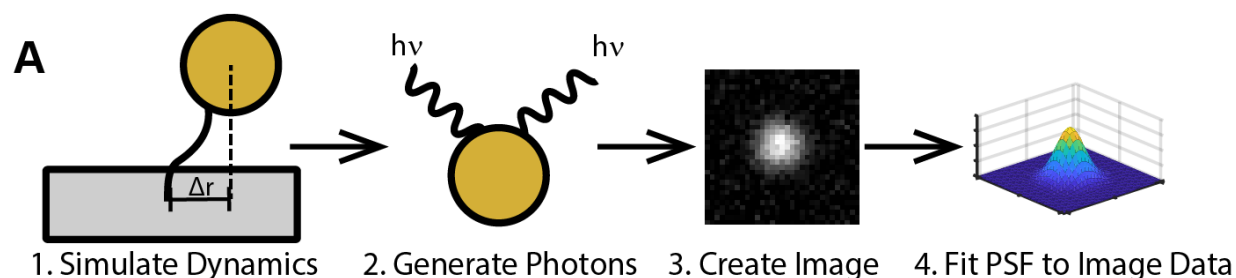
Figure 5. Depiction of the computational workflow. First, the dynamics of the simulation were numerically integrated. Then photons were generated according to a stochastic image generation algorithm. The generated images are fit using a point spread function (PSF) fitting algorithm. The resulting fits of the PSF are analyzed for statistical information regarding the dynamics of the nanoparticle, and protein.

2.2 Brownian Dynamics Simulations

In order to answer questions regarding the limitations and controllable experimental parameters guiding gold nanoparticle tracking assays, a series of Brownian Dynamics models were developed. The first model system involved a gold nanoparticle tethered to a glass slide. The gold nanoparticle was

assumed to be spherical and subjected to a viscous drag force, and an entropic-spring tether extension force, as thermal agitation allowed it to sample its position distribution. The glass slide was modeled as an impenetrable barrier, and the interactions were modeled using a simple hard-wall potential. This model allowed for the characterization of the controllable experimental parameters, including the tether length, tether stiffness, particle size, exposure time, and photon acquisition.

The second model system was a slightly higher degree of computational complexity. In this model system, a 5 nm diameter spherical protein was tethered to a glass slide, and a gold label was tethered to the top of the protein. The protein-gold tether attachment point was allowed to rotate to the side and top periodically, simulating the protein undergoing a periodic conformational change, representing a transition between rotational freedom, and a loss of rotational freedom. The sampling of two distinct positional distributions provided information regarding the effects of particle size on magnifying angular positional changes which do not necessarily correlate with true displacements of the protein. Again, the glass was assumed to be a hard-wall potential, while the collisions between the protein and the nanoparticle were assumed to occur elastically, and were reconciled using conservation of energy and momentum calculations.

The third model was a simplification of the kinesin motor walking on the microtubule. This model allowed for an interrogation of the effects of tether attachment point and structure of the one head bound state on the characteristics of the traces as the kinesin walks on the microtubule. In this model, the underlying physics and kinetics of head attachment, and neck linker displacement were neglected. These factors were instead approximated by exponentially distributed wait times for the two-head-bound state, the ATP waiting state, and the one-head-bound state. In this manner, questions regarding three stepping dynamical models could be compared with actual experimental data, and the underlying structure of kinetic intermediates could be resolved. Volume exclusion was enforced in a similar manner to the second model.
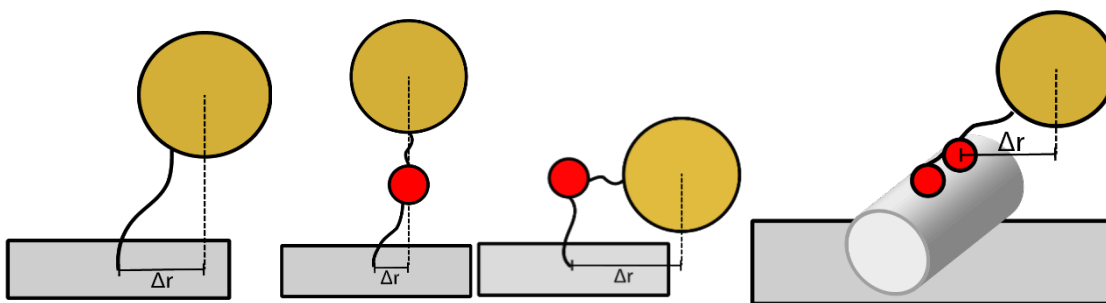
Figure 9 - Depiction of the 3 models considered in this paper. Model 1 (A) Consists of a nanoparticle affixed to a glass coverslip with a polypeptide tether. Model 2 (B) consists of a protein (radius 2.5 nm) affixed to a glass coverslip, with a nanoparticle label attached to it. The nanoparticle tether is free to undergo conformational changes, including change in contour or persistence length, or an altered state of rotational freedom as depicted. Model 3 (C) is an incorporation of the full geometry of *in vitro* motility assays, including a microtubule (radius 12.5 nm) affixed to a glass coverslip, and the kinesin head labeled on the microtubule. This model incorporates a primitive representation of kinesin stepping.

2.2.1 Langevin Dynamics describe the motion of nanoscopic particles

Proteins and other nanometer-scale objects are strongly influenced by random thermal fluctuations. One approach to describe this type of constrained random walk is the Langevin Equation of Motion:

$$m\frac{d^2\vec{r}}{dt^2} - \gamma\frac{d\vec{r}}{dt} + \sqrt{2D}\vec{f}_{therm} = \vec{F}_{spring} \qquad (1)$$

This stochastic differential equation can be interpreted as an application of Newton's Third Law under the assumption of a random forcing, here described by f_{therm}, a zero-mean, gaussian, white-noise process describing the thermal fluctuations of the particle due to the interactions with the solvent molecules. Here, $\gamma = 6\pi\eta r$ is the viscous damping of a sphere with radius r diffusing in a medium with viscosity η. The parameter $D = \frac{k_b T}{\gamma}$ is Einstein's Diffusion Coefficient, with k_b equal to the Boltzmann Constant, and T is the temperature. The deterministic force, $\vec{F}_{spring}$ corresponds to the elastic forces exerted by the polymer tethers in the system.
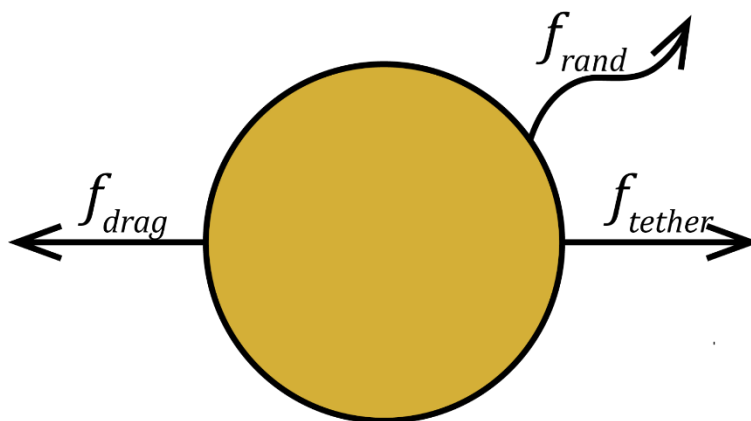
Figure 10 - Free body diagram of the nanoparticle in the overdamped limit. The drag force always opposes the forward motion, while the curved arrow represents the random orientation of the thermal forcing at each timestep.

A key simplification to this equation can be found at very low Reynolds number, as is the case in nanometric systems. In this regime, the viscous damping on the particle dominates the inertial force. Therefore, the acceleration of the particle is sufficiently transient, and the mass of the particle is sufficiently small, that the inertial force $m\frac{d^2\vec{r}}{dt^2}$ can be assumed to be zero, reducing Eq. (1) to the overdamped Langevin Equation of Motion:

$$-\gamma\frac{d\vec{r}}{dt} + \sqrt{2D}\vec{f}_{therm} = \vec{F}_{spring} \qquad (2)$$

In this model, the spring forces were approximated using the worm-like-chain entropic spring model, as polypeptides have been found to be well approximated by this force extension profile[20][21]. This model takes the continuum limit of a freely jointed chain model. Essentially, in order to extend a polypeptide, the reduction in microstates available to the polymer comes with a corresponding loss in entropy. Therefore, an entropic force is exerted such that the polypeptide seeks configurations corresponding to the greatest degree of microscopic degeneracy. This can be approximated mathematically as[22, 23]:

$$|\vec{F}_{spring}| = \frac{k_bT}{4l_p}\left[\left(1-\frac{x}{l_c}\right)^{-2} - \frac{1}{4} + \frac{x}{l_c}\right] \qquad (3)$$

where l_c and l_p correspond to the contour and persistence lengths of the polymer in question, and x equal to the end-to-end distance of the tag. The contour length of the tether describes the maximum extension possible for the polymer, while the persistence length is the rate parameter describing the decay of the tangent-tangent correlation between each point on the polymer. Therefore, longer polymers have a longer contour length, and stiffer polymers (e.g., double stranded DNA or microtubules) have a much larger persistence length. In this model, self-interactions of the tether were assumed negligible, and ignored.

Combining equations (2) and (3), and solving for the velocity of the spherical particle in question leads to the final form of the Langevin equation for a sphere diffusion constrained by a tether,

$$\frac{d\vec{r}}{dt} = \frac{1}{\gamma}\sqrt{2D}\vec{f}_{therm} - \frac{1}{\gamma}\frac{k_b T}{4l_p}\left[\left(1 - \frac{x}{l_c}\right)^{-2} - \frac{1}{4} + \frac{x}{l_c}\right]\hat{x} \quad (4)$$

This first-order stochastic differential equation is discretized and numerically integrated using a modified Euler approach involving the generation of normally distributed random variables for the thermal forcing. This results in the following equation:

$$\vec{r}_{n+1} = \vec{r}_n + \frac{1}{\gamma}\sqrt{2D\Delta t}\vec{N}(0,1) - \frac{\Delta t}{\gamma}\frac{k_b T}{4l_p}\left[\left(1 - \frac{x}{l_c}\right)^{-2} - \frac{1}{4} + \frac{x}{l_c}\right]\hat{x} \quad (5)$$

Where N(0,1) is a zero-mean normal random variable with a variance of 1. This equation is numerically integrated in order to obtain the dynamics of the particles in the system.

2.2.2 Collisions were corrected assuming conservation of momentum and energy

In order to incorporate the steric interactions of the components of the simulation, the internal degrees of freedom of the proteins were neglected, and proteins were coarse-grained as 2.5 nm radius spherical volumes. The nanoparticle was assumed to be a hard sphere with a variable radius depending on the model system under assay, while the microtubule was modeled as a 25 nm diameter cylinder. In order to reconcile the collisions during each iteration, the distances between the simulated objects were

computed. The collision was said to occur if the displacement between the center of the objects $||\vec{d}_{ij}||$ was smaller than the sum of their radii $\sigma_{ij} = r_i + r_j$. This condition is given mathematically as:

$$||\vec{d}_{ij}|| < \sigma_{ij} \quad (5)$$

In order to reconcile collisions, a modified event-driven molecular dynamics (MD) algorithm was used(24, 25). In conventional MD, the position and momentum of each particle in the system is specified for each increment of the simulation. When overlaps occur, the incident kinetic energy and momenta of the particles are used to calculate the post collision position and velocities such that conservation of momentum and energy holds. In the overdamped regime, however, the equation of motion of the particles does not require an explicit definition of the momentum and energy, because the mass is assumed to be equal to zero. In this case, the diffusivity of the particles acts in much the same way as the mass in conventional algorithms.

The resolution of collisions is accomplished as follows. If a collision occurs in the simulation, the minimum displacement, and therefore time of collision, is computed between the objects in the simulation. This is done by assigning a fictive velocity, $\vec{v}_i$ for the objects over the timestep, Δt, such that

$$\vec{v}_i = \frac{\Delta \vec{x}_i}{\Delta t} \quad (6)$$

The collision time, t_c, is found by solving for the good root of the following equation:

$$\left||\vec{d}_{ij} + \vec{v}_{ij} t_c\right|| = \sigma_{ij} \quad (7)$$

Where the variable $\vec{v}_{ij}$ is the relative velocity between the colliding objects, i and j, $\vec{v}_{ij} = \vec{v}_i - \vec{v}_j$. The collision is then mapped to the Brownian center of mass frame, and reflecting the incident velocities along the normal vector between the objects at the time of the collision, and completing the remaining fraction of the timestep, $(\Delta t - t_c)$, with the new, post-collision velocities. The post-collision

velocities can be related to the pre-collision velocities according to the scattering matrix incorporating the diffusion coefficients of the particles, D_i and D_j as follows:

$$\begin{bmatrix} \dfrac{D_j - D_i}{D_i + D_j} & \dfrac{2D_i}{D_i + D_j} \\ \dfrac{2D_j}{D_i + D_j} & \dfrac{D_i - D_j}{D_i + D_j} \end{bmatrix} \begin{bmatrix} v_i \\ v_j \end{bmatrix} = \begin{bmatrix} v_i{}' \\ v_j{}' \end{bmatrix} \quad (8)$$

Thus, the post collision positions of the interjecting objects are calculated as

$$\vec{x}_i' = \vec{x}_i + \vec{v}_i t_c + \vec{v}_i'(\Delta t - t_c)$$
$$\vec{x}_j' = \vec{x}_j + \vec{v}_j t_c + \vec{v}_j'(\Delta t - t_c) \quad (9)$$

2.3 Image Generation and Fitting

Digital cameras rely on the excitation of electrical potential wells through the acquisition of photons during a given exposure window, which is then converted into an intensity value for each pixel. When imaging objects with sizes smaller than the Rayleigh Criterion, the diffraction of photons leads to an Airy Disc diffraction pattern output in the image(11, 26, 27). This diffraction pattern is well approximated by a Gaussian distribution, which is the fact that underlies modern diffraction limited microscopy. Simplified models of these processes were used to create a simulated images, and the resultant images were fit using FIONA methods.

2.3.1 Light scattering by gold nanoparticles is modeled as a stochastic photon emission process

The advantages of gold-nanoparticle tracking mainly stem from the fact that scattering of light by the nanoparticle does not rely on the conventional excitation-relaxation timescale of fluorophores. In order to capture this effect, the nanoparticle dynamics were simulated using the Langevin equation of motion for 1 ms of simulated time. Once the vector of particle positions was obtained, the (x,y)

coordinates of the particle were subsampled to the desired exposure time window. The scattering of

photons during each simulation timestep was modeled as a Poisson process characterized by a mean

number of photons per time step (1 ns), determined such that the desired saturation of the frame was

accomplished by the end of the exposure time window. The photons were then distributed to various

positions on an artificial pixel grid corresponding to a normal random variable with standard deviation

calculated from the full-width at half maximum (275 nm) of the point spread function of the imaging

apparatus. When the photons were distributed to their various positions, they were then binned in to a 30

x 30 pixel grid, with each pixel measuring 37.4 nm wide. The photon counts were converted into 10 bit

images by turning photon counts into bit values, and then saving the image as a 16 bit image. A sample

image is depicted in Figure 11.
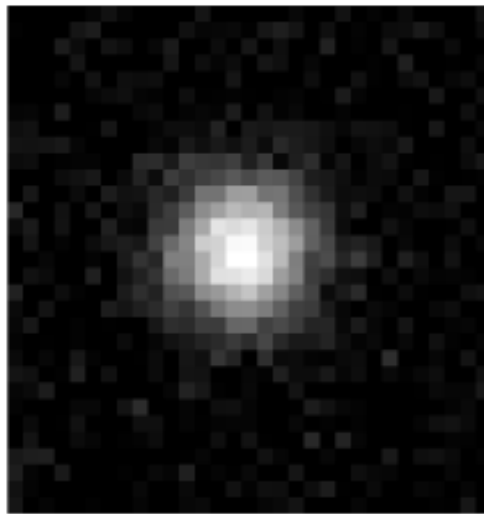
Figure 11 – Example frame generated by the imaging algorithm.

2.3.2 Images were fit using a 2D Gaussian Distribution

The images generated according to the algorithm detailed above were fit using Fluorescence

Imaging Evaluation Software for Tracking and Analysis (FIESTA)(27). This software uses a least-

squares fitting of a Gaussian distribution to the convolution of the object and the point spread function of

the imaging apparatus. From this fit, parameters including the width of the diffraction pattern, and,

importantly, the mean position are extracted. Therefore, the position of a point source can be

interpolated. These position vectors can be extracted and analyzed for the relevant statistics, including

the root mean squared error, and the critical exposure time for imaging.
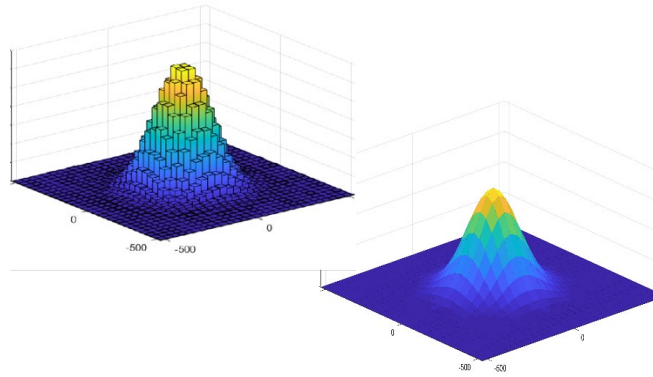
Figure 12 - Idealized depiction of the image fitting process. The
left is the raw intensity data taken from the image. The algorithm
takes this intensity data and fits a gaussian profile to it, from which
the relevant parameters are taken

Chapter 3

Results

3.1 Assessing the Contribution of Experimental Parameters to Point Spread Function Fitting Fidelity

3.1.1 Fidelity of PSF fitting is strongly influenced by photon count and exposure time

To investigate the conditions under which point-spread function fitting is an unfaithful reporter of positional information, Model System 1, the simplified model of tethered particle diffusion on a glass surface, was used. In order to assess the contribution of fluorescence intensity to the imaging error, the photon count per acquisition period was varied from 0.3 photons per nanosecond up to 1.6 photons per nanosecond. Particle position was updated every 1 nsec. The other experimental parameters were here held constant, with the contour length (l_c) equal to 11.4 nm, the persistence length (l_p) equal to 1 nm, and gold diameter (D_{gold}) equal to 30 nm. The exposure time was held constant at 600 μs, and the frame rate was fixed at 1000 frames per second. These data were analyzed, and the standard deviation from the mean tether attachment point on the glass surface was calculated for each photon flux. The relationship between the standard deviation and photon count scaled as $1/N$ in the low photon regime, and then transitioned to a $1/\sqrt{N}$ law at higher photon counts when background noise becomes negligible compared to the strength of signal. An interesting observation was that the fitting process continued to increase in tracking fidelity, even in the case where the frame became oversaturated. This suggests that, in order to capture low variance image signals using gold-labeling, maximizing emission intensity should be prioritized.

To address whether the fitting process can work at arbitrarily high frame rates, the above simulation was repeated, this time holding photon count constant such that the center pixel remained fully saturated regardless of camera exposure time. The exposure time was changed in logarithmically spaced increments from 1 μs to 950 μs in order to assess the point at which tracking became unreliable. It was observed that decreasing the exposure time past a certain point necessarily caused increase in the standard deviation of the signal. This phenomenon can be understood by considering the dynamics of the particle as it explores all the configurations available to it. If the particle is not allowed adequate time to sufficiently explore its distribution, then the photons emitted do not capture the central tendency of the distribution, and the reliability of tracking suffers. This process is depicted in Figure 14. To quantify the exposure time dependent loss in tracking accuracy, a parameter, here called the critical exposure time, or t_{crit}, is introduced as a way to measure the transition between reliable and unreliable tracking. This parameter is defined as the exposure time at which the standard deviation of the fitted position rises above 10% of the baseline value. The takeaway from the strong exposure time dependence of the standard deviation is that gold-nanoparticle tracking cannot be extended to arbitrarily high framerates because of the time required for the nanoparticle to truly approximate a point source of radiation, even in the case where the experiment is not photon limited. Therefore, in any gold labeling experiment, accurate images require a carefully chosen exposure time such that the nanoparticle is an accurate reporter of the protein position.
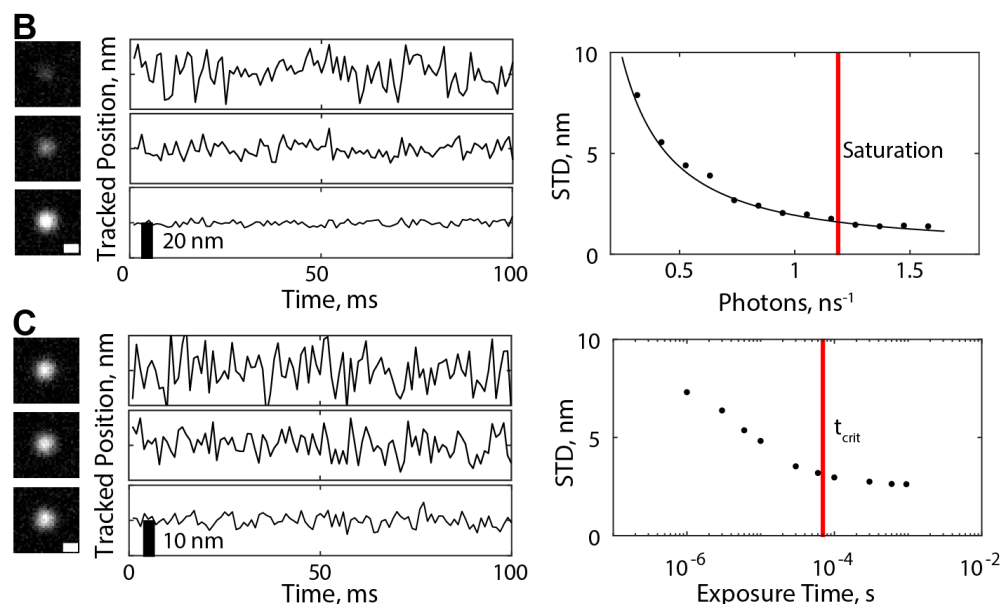
Figure 13 – The image signal remains noisy in the photon limited, and exposure time limited regime. **(A)** Artificial images and fitted position run with $l_c = 12$ nm, $l_p = 1$ nm, $D_{gold} = 30$ nm, exposure time equal to 600 μs, and f = 1,000 fps with the timestep equal to 1 ns. The sample images show (top to bottom) photon rates of 0.3, 0.6, and 1.5 photons per nanosecond, respectively. The tracking fidelity was quantified as standard deviation of the position over the 100 ms traces. The black line shows a fit to $\frac{a}{x} + \frac{b}{\sqrt{x}} + c$, $R^2 = 0.994$. The vertical line represents the point at which the center pixel of the image was saturated.
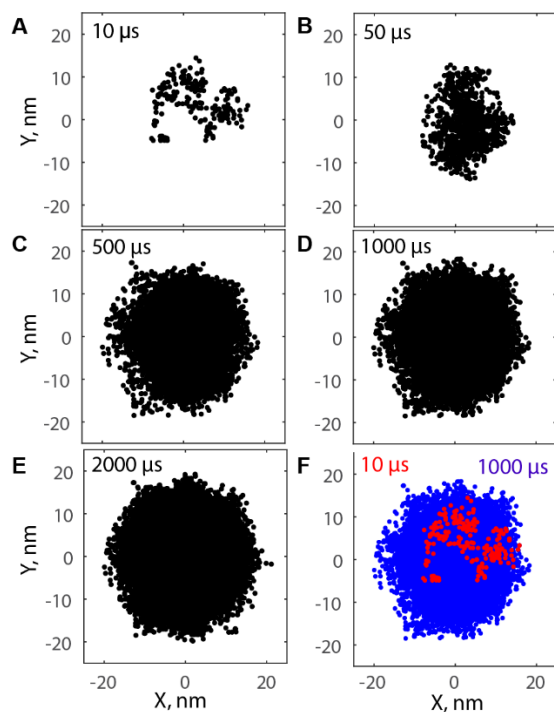
Figure 14 -The critical exposure time requires the nanoparticle to fully explore its distribution. Particle position was updated every 1 nsec, and distributions of particle position are depicted for **(A)** 10 μs, **(B)** 50 μs, **(C)** 500 μs, **(D)** 1000 μs, and **(E)**

2000 μs exposure times. **(F)** Comparison of the 10 μs and 1000 μs distributions demonstates that the 10 μs exposure has undersampled the final distribution, while 1000 μs has fully explored the available space.

3.1.2 Contour Length and Particle Size strongly influence tracking fidelity, while persistence length has a lesser impact

In order to guide best practices regarding the choice of tagging strategies for the protein in question, the effects of particle size, contour length, and persistence length on the critical exposure time were investigated. To do this, Brownian Dynamics simulations were conducted with various contour lengths, persistence lengths, and particle sizes. The contour lengths spanned from 2.91 nm, representing a short chemical conjugation method, to 30 nm, longer than the length of an antibody tag. The persistence lengths explored spanned from 0.2 nm, a lower physical bound on the persistence length of polymer tethers, to 2 nm, which is roughly the persistence length of single-stranded DNA (28, 29). It was found that the contour lengths and the nanoparticle size had the largest impact on the critical exposure time. The physical basis for this result can be understood by considering that increasing the contour length leads to a larger available volume for the particle to explore, requiring a larger time for the particle to fill out its distribution. Similarly, increasing the particle size leads to a larger positional distribution due to the increased radius and therefore larger volume sampled by the particle, while the decrease in diffusivity with increasing particle radius slows the exploration of the conformational microstates. The persistence
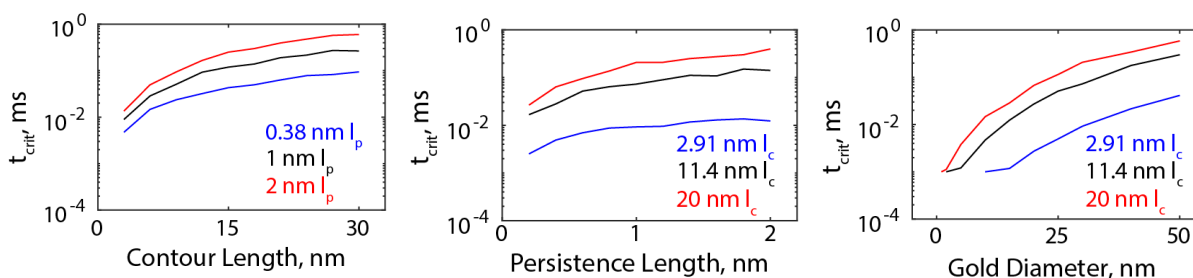
Figure 15. The critical exposure time has a stronger dependence on contour length and gold diameter than on persistence length. Critical exposure time versus **(A)** contour length, **(B)** persistence length, **(C)** gold particle diameter. The changes in critical exposure time span roughly 2 orders of magnitude for contour length, 3 orders of magnitude for particle size, and 1 order of magnitude for persistence length, indicating that, for good correspondence between the label and the protein, contour length and particle size should be minimized as much as possible.

length, while having some impact on the critical exposure time, did not have anywhere near the impact of

the other two parameters. Taken together, these results indicate that very tight protein-label strategies should be used when available, and the particle size should be minimized as much as possible when designing the experiment.

3.2 Exploring the effects of protein conformational changes and collisions on tracking fidelity

3.2.1 Increasing the tether length does not impact tracking, provided a proper exposure time is chosen

While assessing the effects of contour length on the critical exposure time, it was noted that reliable tracking requires tight conjugation strategies. However, in many cases, proteins undergo time dependent conformational changes that result in changes in the positional distribution due to changes in the tethered freedom of the protein. Therefore, a model was developed to assess the conditions under which the point spread function fitting process could distinguish between different distributions. Using the Model 1 system geometry, 2 distributions of a long (l_c =20 nm, l_p = 1.6 nm) and short (l_c = 9 nm, l_p = 0.38 nm) tether were sampled. The distributions are depicted in Figure 16A. A thought experiment was performed with these two configurations using a time dependent conformational change between the short and long tether every 25 ms. These choice of tether parameters results in a tenfold change in critical exposure time, allowing for a carefully selected exposure time to discriminate between the two structural states. Brownian Dynamics simulations of this model were performed at several exposure times, and the resulting images were fit using FIESTA. The fitted positions and standard deviations for three exposure times are depicted in Figure 16B.

In the case where the exposure time was less than the critical exposure for both conformations, the particle was a poor approximation of a point source for both conformational states, and the positional variance for each state was too high to reliably distinguish the states. Conversely, if the exposure time was longer than the critical exposure time for both of the conformations, the particle approximated a point

source for both states, and the corresponding decrease in positional variance made the two states indistinguishable. If the chosen exposure time lies between the critical exposure times for the two states however, the lower critical exposure time state observes a decreased positional variance, while the variance of the higher critical exposure time state remains high, meaning that the unfolded and folded states can be inferred from the change in variance of the signal. In this case, the shorter tether length was an accurate approximation of a point source of radiation, while the longer tether continued to undersample its positional distribution. The implication of this result is that gold tracking experiments may be used to detect fairly rapid conformational changes in protein structure without positional displacements, provided a carefully chosen exposure time is used. This exposure time may be difficult to select *a priori*, and therefore experiments could require multiple exposure times to determine this "Goldilocks Zone" of structural change detection.
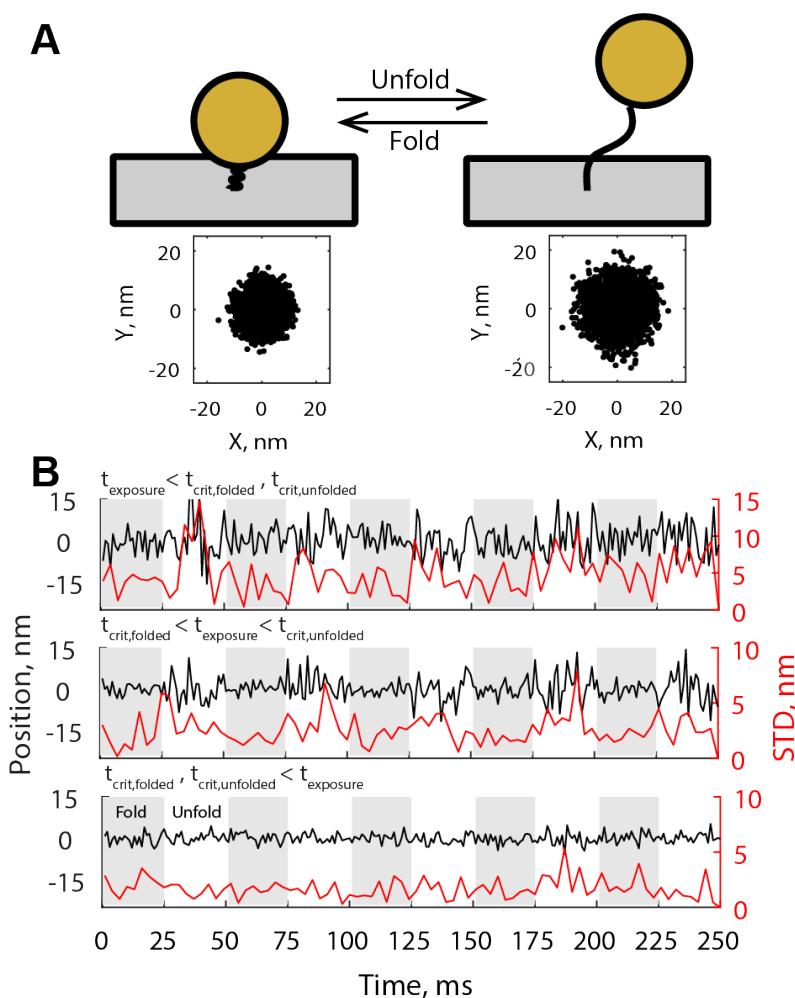
Figure 16. Resolution of protein conformational changes via PSF fitting depends on exposure time. (A) (Top) Model system where a protein tagged with a 30-nm gold nanoparticle switches between a folded ($l_c = 9$ nm, $l_p = 0.38$ nm) and unfolded state ($l_c = 20$ nm, $l_p = 1.6$ nm). (Bottom) Distributions of nanoparticle positions in the folded (left) and unfolded (right) state. (B) Example nanometric tracking data from a protein that cyclically folds and unfolds, tested at three different exposure times (1 µs, 10 µs, and 950 µs) and a camera frame rate of 1,000 frames per second. Standard deviation (STD) was assessed using a 3-frame boxcar.

3.2.2 Shorter tethers increase the collision frequency between the protein and gold nanoparticle

While shorter tethers decrease the critical exposure time, the size of the nanoparticle relative to the protein (~ 6 times larger) raised questions about whether bringing the nanoparticle in closer proximity to the protein would exert steric effects on the natural dynamics of the protein.   To probe this question, Model System 2, the double tethered diffusion on a glass slide simulation, was employed. The protein

was modeled as a 5 nm diameter sphere tethered to the glass surface with a 10.4 nm contour length tag, while the nanoparticle remained a 30 nm sphere tethered to the protein via a variable contour length tag. This model approximates a tagging experiment involving a single protein domain attached to another domain via a disordered polypeptide region like a kinesin protein in a one head bound state. Collisions were enforced assuming conservation of energy and momentum in the overdamped regime, as described in section 2.2.2. The distributions of both the nanoparticle and protein were sampled for both a short tether (2.91 nm, corresponding to a biotin-PEG-maleimide linkage)(30), and a long tether (11.4 nm, corresponding to the 31 amino acids comprising the N-terminal cover strand and AviTag of kinesin-1)(7, 31), and are depicted in Figure 17BAs is expected, the longer tether produces a much broader distribution than the shorter, recapitulating the benefits of tight tether moieties for higher framerate tracking.

As a control experiment, both tether cases were simulated in the absence of inter-particle interactions in which the protein and particle were allowed to freely diffuse through each other. When collisions were enforced, the statistical properties of the distribution were unaltered, indicating that the nanoparticle does not, in general, strongly disrupt the protein dynamics, validating the use of gold labels as a way to interrogate natural protein function.

To quantify the dependence of collisions on contour length, the collision frequency per time step (1 ns) was calculated. Unsurprisingly, longer tethers produced far smaller rates of interactions, with rates of 0.05 collisions per nanosecond in the 15 nm case, whereas a sharp increase to roughly 0.3 collisions per nanosecond was observed in the shortest, 3 nm case. While the shorter tether provides more faithful tracking of protein dynamics, it does so at the expense of increasing the interactions between the protein and the probe.
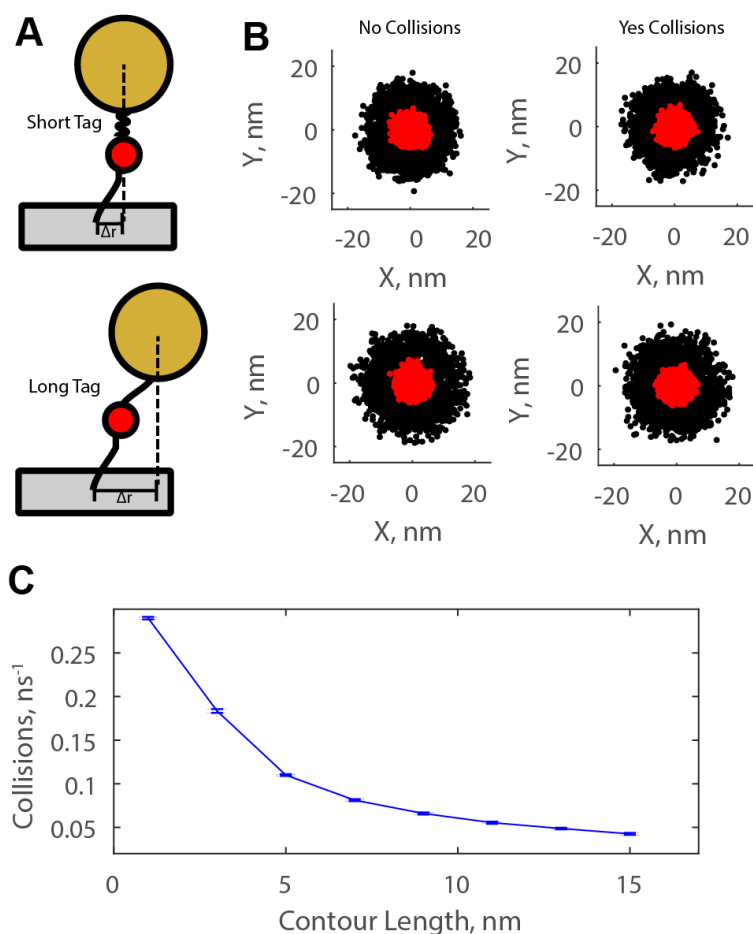
Figure 17. Tethers with shorter contour lengths lead to more frequent collisions between the gold nanoparticle and the tagged protein. (A) (Top) Diagram of the double tethered diffusion system. The tether between the glass and the protein has a constant $l_p = 1$ nm and $l_c = 10.4$ nm. The tethers between the protein and the gold have $l_p = 1$ nm and $l_c = 2.91$ nm (short) or 11.4 nm (long). (B) Distributions of both the protein (red) and the nanoparticle (black) for short (top) and long (bottom) tethers generated in BD simulations. Collisions between the nanoparticle and the protein were allowed in the left column, but not the right column. (C) The number of detected collisions between the nanoparticle and the protein as a function of tether contour length. Error bars represent mean $\pm$ SEM for N = 30 measurements.

3.2.3 Changes in rotational freedom of the protein can cause large apparent displacements in particle positions

To assess the impact of protein structural constraints on tracking, again, Model System 2 was employed. In this case, the protein-tether attachment point was fixed on the surface of the protein. The tether attachment point was fixed to the top of the protein, simulating a case of rotational freedom of the

protein, and displaced to the one side of the protein, simulating a structural constraint on the diffusion of

the mechanical element of the protein. The configuration of the system was switched back and forth

between these structural states to simulate the protein losing and gaining rotational freedom (Figure 18A).

This model system is especially relevant to understanding the dynamics of tracking processive enzymes,

like kinesin, which undergo periodic transitions between strong binding to their substrate, in which the

protein-tag attachment point is rotationally constrained, to weakly associated, or fully dissociated states,

in which the tether position rotates freely as the protein undergoes tethered diffusion. In these situation,

rotation of the protein and the tether point of the tag can give rise to artifactual displacements that do not

correlate with actual protein displacements. Therefore, it is important to characterize and understand the

ways to experimentally mitigate these erroneous readouts.

This computational experiment was conducted with a 5 nm protein labeled with a 40 nm

nanoparticle, conjugated using a 2.91 nm contour length, 0.38 nm persistence length. Distributions for

these parameters are depicted in Figure 18B. Brownian Dynamics simulations of the switching process

were conducted, allowing the system to switch between the rotationally free state and constrained state

every 10 ms. Images were collected at an exposure time of 100 μs at a frame rate of 1000 fps, and

analyzed to quantify the positional bias, Δx, depicted in Figure 18C. The interactions between the head

and nanoparticle introduce a sizable positional bias in the X direction, despite the mean protein position

remaining invariant with time. These results suggest that large angular changes in structure, or transitions

between rotationally constrained and rotationally free protein conformations, can produce artifactual

displacements that do not correlate with true protein positional changes.

To quantify the relative contribution of experimental conditions on the observed positional bias,

the same experiment was conducted while varying the label contour and persistence length, and the

nanoparticle diameter. The experiments suggest that varying persistence length only weakly alters the

observed positional bias (Figure 18D). Alterating the contour length were found to have a much more

sizable effect on the observed positional bias, with the magnitude of the rotational artifactual translations

decreasing with increasing contour length (Figure 18E).   Finally, increasing gold size demonstrated a very strong influence on the observed artifactual translations – decreasing the particle size to angstrom scale, on par with organic fluorophores often used to label proteins, almost completely abolished the apparent displacements (Figure 18F). Taken together, these results recapitulate the previous result that minimizing the particle size should be prioritized in any experiment. However, in contrast with the previous recommendation for shorter tagging strategies for accurate tracking, if the protein undergoes large rotational state changes, it may be prudent to use a longer contour length tether to mitigate the rotation-induced false displacements.
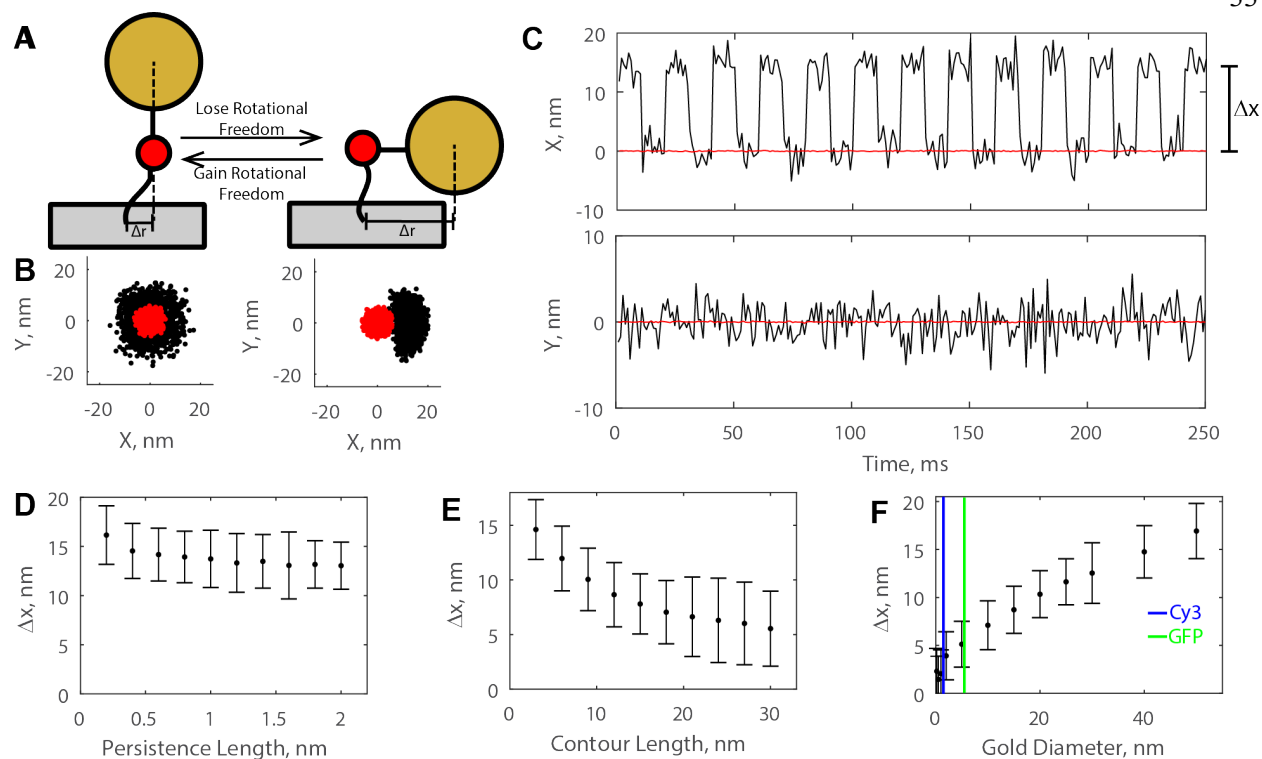
Figure 18. Changing rotational freedom can produce artifactual translations in nanometric tracking of gold nanoparticle-tagged proteins. (A) Double tethered diffusion system, where the rotational freedom of the tagged protein can be gained or lost by freeing or fixing the protein-gold tether connection point. (B) Distributions of protein and gold nanoparticle positions. Losing rotational freedom biased the position of the gold (black) to one side of the protein (red). Both BD simulations run with run with l_c = 2.91 nm, l_p = 0.38 nm, D_{Gold}= 40 nm, t_{expose}=600 μs, and f = 1,000 frames per second. (C) Nanometric tracking data of a system that switches between high and low rotational freedom (matching panel B) every 10 ms. Clear artifactual translations of magnitude Δx occurred whenever the system switched. (D) Magnitude of the artifactual translation tested at multiple persistence lengths, all with l_c= 2.91 nm, D_{Gold}= 40 nm, t_{expose}=600 μs, and f = 1,000 frames per second. Each point shown mean ± STD for N = 100 simulated switches. (E) Magnitude of the artifactual translation tested at multiple contour lengths, all with l_p = 0.38 nm, D_{Gold}= 40 nm, t_{expose} = 600 μs, and f = 1,000 frames per second. Each point shown mean ± STD for N = 100 simulated switches. (F) Magnitude of the artifactual translation tested at multiple nanoparticle diameters, all with l_c = 2.91 nm, l_p = 0.38 nm, t_{expose} = 600 μs, and f = 1,000 frames per second. Each point shown mean ± STD for N = 100 simulated switches. Diameters of an organic dye (Cy3) and green fluorescent protein (GFP) are shown for reference.

3.3 Assessing kinesin-1 tracking experiments using a simplified mechanochemical model

3.3.1 Different kinesin-1 labeling positions lead to different characteristic stepping patterns

The introduction of gold-nanoparticle tracking experiments to single-molecule, kinesin motility, assays has provided insight into the very rapid structural transitions in kinesin stepping. While conventional fluorescence experiments suggest 16.4 nm translocation in the head position per kinesin step(6), high frequency gold tracking suggests the existence of substeps as the protein waits for an ATP dependent translocation(7, 8). However, label-dependent discrepancies in stepping dynamics appear to suggest very different structures for the ATP waiting state of the motor. In particular, labeling the head with an N-terminal Avi-Tag, or to the rightward side of the head (Figure 19C), suggests a two-heads-bound structure to the ATP waiting state, wherein the head is undisplaced, and the binding of ATP then detaches the head, and translates it to the next tubulin binding location(7). Labeling on the S55 location, or the rear of the bound head (Figure 19A), suggests a 1 head bound intermediate in which the freed head passively transitions forward and rightward from the previous binding site, and the binding of ATP then completes the transition forward to the next binding site(8). A puzzling third pattern that emerges in the case of an E215, or forward displaced (Figure 19B), labeling strategy suggests a 1 head bound intermediate state wherein the head waits for ATP translated backward and rightward from the binding site, and then ATP binding translates the head to the next binding site. These apparently contradictory

patterns suggest fundamentally different kinesin stepping mechanisms. Therefore, resolving these

discrepancies is crucial to elucidating the mechanochemical cycle of kinesin-1.
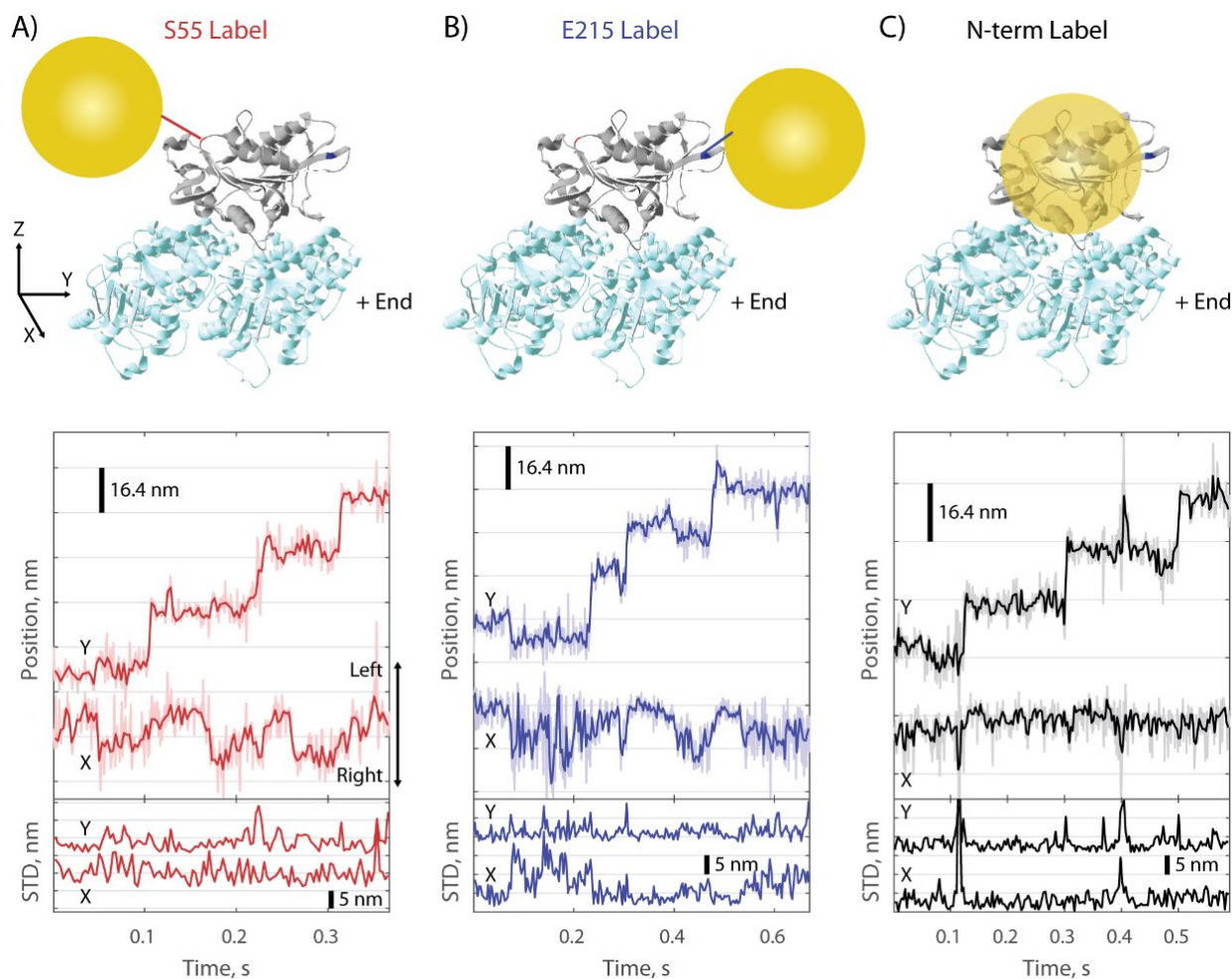
Figure 19. Experimental high-resolution gold nanoparticle tracking at low ATP shows that the apparent position of the ATP waiting state depends on the gold nanoparticle attachment position. (A) Cys-Lite with a cysteine introduced at S55 (red). As shown from the crystal structure, this tag position puts the gold nanoparticle on the rear-center of the kinesin head. The stepping trace shows clear movements to the lateral (X) right of the MT accompanied with increased fluctuations (3-frame boxcar standard deviation, STD) and small displacements along the microtubule axis (Y) during the ATP waiting state. (B) Cys-Lite with a cysteine introduced at E215 (blue). As shown from the crystal structure, this tag position puts the gold nanoparticle on the front-center of the kinesin head. The stepping trace shows clear movements to the lateral right accompanied with increased fluctuations and consistent backward displacements along the microtubule axis (Y) during the ATP waiting state. (C) N-terminus biotinylated *D. melanogaster* K560-AviN (black). As shown from the crystal structure, this tag position puts the gold nanoparticle on the right side of the kinesin head. The stepping trace shows no clear movements in X or Y during the ATP waiting state, nor are increases in fluctuations evident. Sudden spikes in STD are sudden losses in tracking precision to free-diffusing gold nanoparticle overlapping with the walking kinesin. All dark colored traces are downsampled with a median or STD boxcar from 1,000 to 333 frames per second. Gold nanoparticles (30 nm) are not drawn to scale. Experimental data taken by Keith Mickolajczyk. Crystal structure of human kinesin in the no-nucleotide state on microtubules (PDB 3j8X) from Shang and Sindelar.

3.3.2 Simulated kinesin traces suggest a rotationally free, but longitudinally undisplaced ATP waiting state

In order to explain the differences in observed stepping patterns between each tagging strategy, three potential models of the ATP waiting states were proposed, and tested using Brownian Dynamics simulations. In the *unbound-displaced* model, the ATP waiting state is characterized by a full release of the stepping head from the rear tubulin binding location, followed by a passive relaxation into a true one head bound state in which the head has access to full rotational freedom. In the *unbound-undisplaced* model, the rear head is rotationally free, but does remains weakly associated near the rear binding site. In the *bound-undisplaced* model, the rear head does not dissociate from the rear binding location, and therefore remains constrained to the microtubule surface. These stepping models are depicted in Figure 20A.

To simulate the three possible models, a kinesin stepping model incorporating the full geometry of the head on the microtubule was employed. The kinesin head was approximated using a spherical volume of 5 nm diameter, the nanoparticle by a spherical bounding volume of 30 nm diameter, while the microtubule was approximated as a cylindrical bounding volume of diameter 25 nm. The motor was stepped in the top center protofilament. The conjugation strategy used in these simulations was a 2.91 nm contour length, 0.38 nm persistence length tag attached to the S55, E215, and N-terminal attachment points. In order to approximate the geometry of these tags, the tether attachment point in the 2 heads bound state was assumed to lie on the kinesin head surface at a height of 2.5 nm above the microtubule, displaced by 2.5 nm to the rear (S55), front (E215), and right (N-Terminal) of the head's center. To simulate steps, the motor was stochastically switched between a bound state, in which the head is rigidly attached to the microtubule, and an unbound state in which the head is bound to the right-hand surface of the second microtubule bound head through the neck linker, which is here assumed to be a 28 amino acid polypeptide with a 10.4 nm contour length, and a 1 nm persistence length (23). When the head was bound, the tether attachment point was fixed in place. Upon transitioning to an unbound state, the tether

attachment point on the unbound head was freed, simulating access to rotational freedom. To simulate

this rotational freedom, the direction between the head and nanoparticle were computed, and the tether

point was then assumed to lie on the minimum translational vector between the nanoparticle and the

unbound head.

Each ATP waiting state was simulated as follows. In the *unbound-displaced* model, the labeled

head was translated forward by 8.2 nm into a rotationally free state. In the *unbound-undisplaced* case, the

head was not translated along the microtubule, but was completely rotationally free. For the final, *bound-*

undisplaced model, no translation was enforced on the head, and it was assumed to remain rigidly

attached to the rear binding site. The dynamics of the ATP independent translation of the motor was

neglected, because it is sufficiently transient relative to the ATP dependent waiting state to be considered

negligible. The step was completed by translating the head forward by 8.2 or 164 nm

Each ATP waiting state was simulated as follows. In the *unbound-displaced* model, the labeled

head was translated forward by 8.2 nm into a rotationally free state. In the *unbound-undisplaced* case, the

head was not translated along the microtubule, but was completely rotationally free. For the final, *bound-*

undisplaced model, no translation was enforced on the head, and it was assumed to remain rigidly

attached to the rear binding site. The dynamics of the ATP independent translation of the motor was

neglected, because it is sufficiently transient relative to the ATP dependent waiting state to be considered

negligible. The step was completed by translating the head forward by 8.2 or 16.4 nm. In the unbound

states, the free kinesin head was displaced laterally to the right, to the location of the adjacent

protofilament. This was accomplished by moving the head to the adjacent protofilament, 6.97 nm to the

right, and 0.78 nm down on the microtubule. This value was calculated by assuming that each

microtubule protofilament accounted for 1/13 of the circular microtubule, and the displacement was

computed using trigonometric relations. The existence of such a lateral displacement is not an

unreasonable supposition, because structural data indicates that the neck linker emerges from the right

side of the bound, unlabeled head(32). Simulated steps were generated, and analyzed using FIESTA. The results of these trajectories are depicted in Figure 20B.

In comparing the simulated data to the experimental traces, it is evident that only the *unbound-undisplaced* model is able to replicate the experimental trajectories. The key feature of theses stepping patterns are described in Table 1. For the *bound-undisplaced model,* the lack of rightward translations in the S55 and E215 simulated traces indicates that this model does not capture key features of the ATP waiting state. For the *unbound-displaced* model, there is an observed 8.2 nm substep in the N-Terminal label that is not experimentally observed, while the S55 and E215 do not display robust forward or backward translations, respectively. This contrasts with the *unbound-undispalced* model, where the N-Terminal tag displays no rightward displacements or 8.2 nm substeps, and is consistent with the experimental observations. Similarly, the S55 and E215 tagging locations recapitulate the rightward bias in the ATP waiting state, while also displaying forward (S55), and backward (E215) substeps upon transitioning into the ATP waiting state. This result indicates that the structure of the ATP waiting state of kinesin is best described as being *unbound,* and *undisplaced* longitudinally from the previous binding location, and that the observed differences in stepping patterns can be explained due to the differences in labeling position. This result underscores the fact that it is necessary to carefully consider the structural constraints on the tethered diffusion of the nanoparticle when interpreting gold labeling experiments, as failing to account for rotational constraints can lead to erroneous conclusions.

Table 1. Summary of the apparent position of the rear head in the ATP waiting state for multiple tagging strategies. Only the *unbound-undisplaced* simulated data matched the experimental data.

	S55 (back)		E215 (front)		N-term (right side)	
	Y	**X**	**Y**	**X**	**Y**	**X**
Experimental	Forward	Right	Backward	Right	None	None
Bound-undisplaced	None	None	None	None	None	None
Unbound-undisplaced	Forward	Right	Backward	Right	None	None
Unbound-displaced	Forward	Right	None	Right	Forward	None
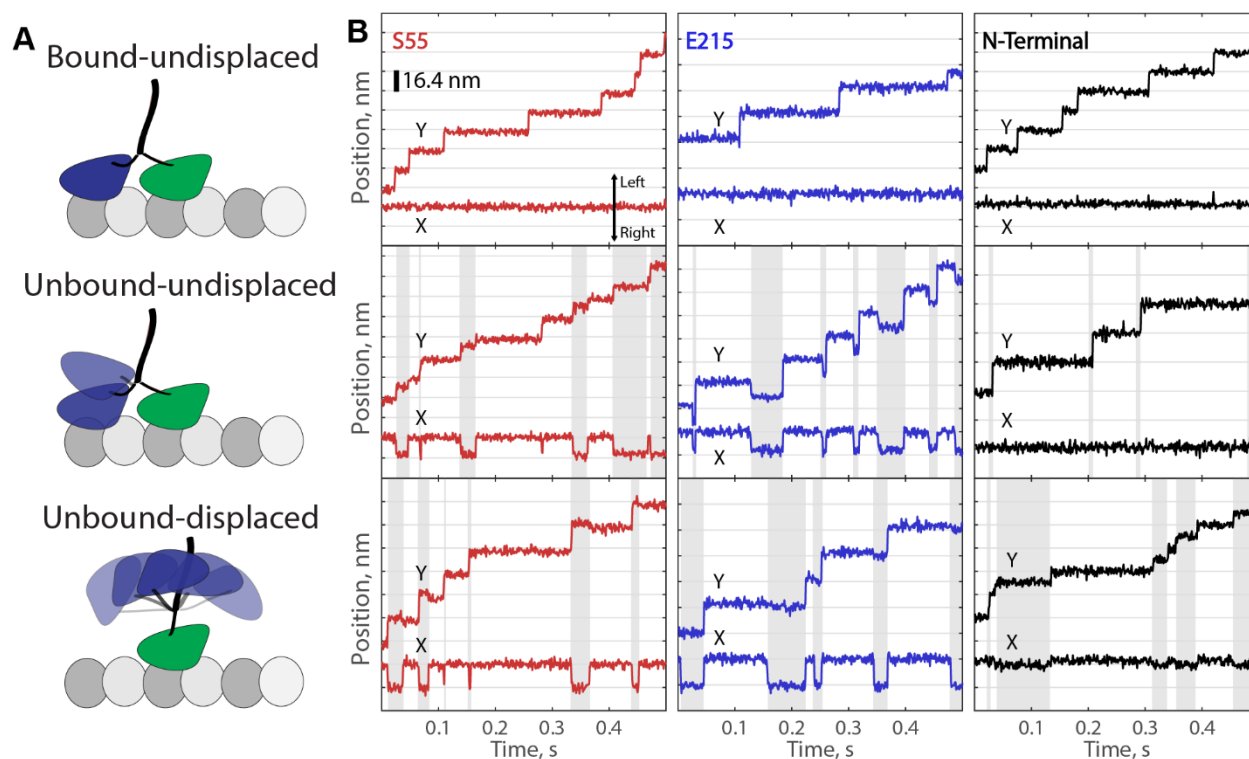
Figure 20. Simulated kinesin stepping best supports an *unbound-undisplaced* ATP waiting state. (A) Schematic showing the position of the tracked (blue) head in three different potential head configurations during the ATP waiting state. (B) Simulated tracking data for the S55 (red), E215 (blue), and N-terminal (black) labeling positions at low ATP and assuming the corresponding configuration for the ATP waiting state from (A). Gray shading indicate that the labeled head is unbound from the microtubule. Only the *unbound-undisplaced* model matched the experimental data for all three tag positions.

Chapter 4

Discussion

In this work, a Brownian Dynamics model was used to quantify the reliability of high frequency gold-nanoparticle tracking. Using a simplified model of tethered diffusion, the key experimental parameters that influence the tracking error were identified: tether contour length, particle size, and exposure time. It was discovered that, in order to reliably detect structural changes in a protein, the exposure time must be chosen such that it captures the difference in the variance of tethered diffusion in the two states.

 Using a second model system involving the tethered diffusion of a protein tethered to a glass slide, the effects of collisional and rotational dynamics were considered. It was found that, while shorter tethers have the benefit of more faithful tracking, they come at the expense of increased collisional frequencies between the protein and the probe. However, the data indicate that the presence of the gold nanoparticle does not significantly impact the underlying distribution, and therefore natural dynamics, of the protein. Importantly, a caveat on the interpretation of experimental tracking data was identified in the case where the protein in question undergoes rotational conformational changes, or has a highly rotationally constrained state. In these cases, it is found that observed displacements do not always correlate with true displacements of the protein, and so known structural data should be considered when interpreting gold nanoparticle tracking results.

The lessons learned using the simplified models of gold nanoparticle tracking were then applied to explaining observed discrepancies in the stepping pattern of kinesin-1, particularly as they pertain to the ATP waiting state of the motor. It was found that label-dependent changes in the dynamics of kinesin-1 can be largely explained by considering the rotational constraints on the motion. A Brownian Dynamics model of kinesin stepping suggests that as the leading head waits for ATP, the trailing head is unbound and rotationally free, but undisplaced from its previous tubulin binding site. Furthermore, it

appears that the head swings to the right during stepping. These results highlight the importance of considering the underlying dynamics of the gold nanoparticle, and thestructure of the protein when designing experiments to assay temporally sensitive changes in protein structure.
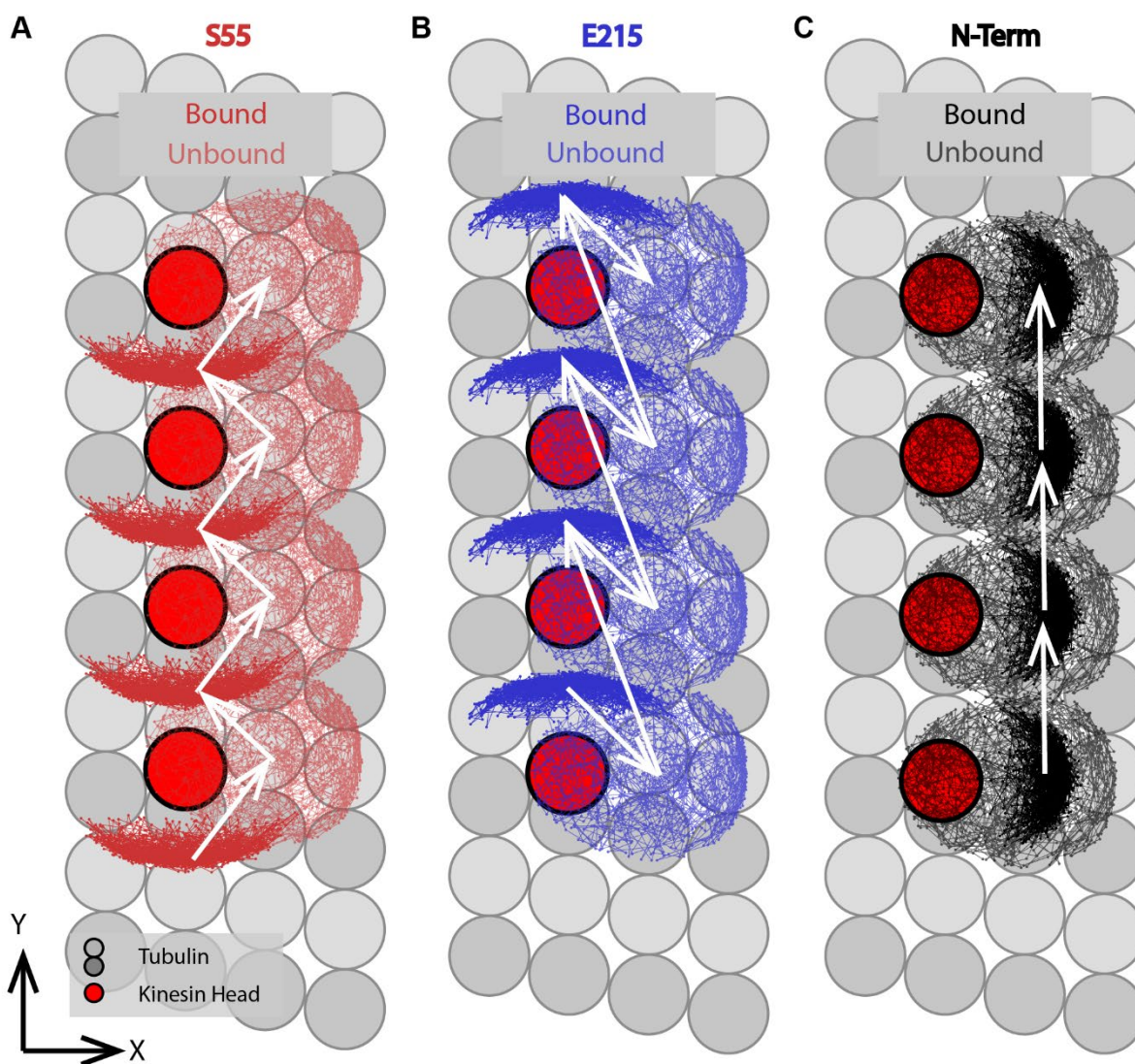
Figure 21. Characteristic distribution of the nanoparticle during several steps of the model *unbound-undisplaced* kinesin stepping pattern. Red circles denote the successive locations of the labeled kinesin head when bound to the microtubule. White arrows denote translations of the nanoparticle distribution. The (A) S55 (red) labelling position (rear of head) shows a clear rearward bias in the 2HB state, with a transition forward and to the right as the head enters the ATP waiting state, while the (B) E215 (blue) labelling position (front of head) shows a clear forward bias in the 2HB state, with a transition backward and to the right as the head enters the ATP waiting state. (C) The N-Term (black) labelling position (right side of head) has a rightward bias throughout the step of the kinesin. The rightward transitions of the labeled head are counteracted by the inherent rightward bias of the N-Term label in the 2HB state. Each data point represents 1 µs.

Taken together, the results presented here represent guidelines for experimentalists as the function of other mechanoenzymes, such as dynein, myosin, polymerases, or cellulases are probed using gold nanoparticle tracking experiments and PSF fitting. Experimentalists should work to optimize exposure time to their specific application, conjugate the protein using an advantageous labeling strategy, and to remember that what you see is not always what you get.

Appendix A - Sample MATLAB Code for Brownian Dynamics Simulations and Imaging

```matlab
% Files holding the dynamical variables and polymer variables
load('dynamicalVariables.mat')
load('polymerVariables.mat')

% Code illustrating model 1 with steps and sample imaging

numFrames = 10;
T = 1E-3;
    dt = 1E-9;
    n = round(T/dt);

for equilibriumPoint = 0:8.2:15*8.2

    for i = 1:numFrames
        % Initial conditions of the nanoparticle are randomized
        if i == 1 && equilibriumPoint == 0
            nanoPosition = [5.2*randn  zeros(1,n)
                            5.2*randn  zeros(1,n)
                            (1.22*randn + 15.5) zeros(1,n)];
        else
            nanoPosition(:,1) = nanoPosition(:,end);
        end

        nanoForce = zeros(3,n);

        nanoRadius = 15;

        % Calculate the drag coefficient and einstein relation for the
        % nanoparticle
        dragCoeffNano = 6*pi*viscosity*nanoRadius;

        nanoDiffusionCoeff = kBoltz*tempKelvin/dragCoeffNano;

        % Pre initialize the random variables associated with the diffusion
        % of the particles
        nanoBrownian = sqrt(2*nanoDiffusionCoeff*dt)*randn(3,n);

        % Declare the contour lengths and persistence lengths of the
        % polymers
        contourLengthTag = contLengthAviTag;

        persistenceLengthTag = persLengthAviTag;

        % Noise standard deviation for the dark current of the images,
        % determined empirically
        noiseStandDev = 4000;

        for k = 1:n
```

```matlab
            [~,magnitude,direction] = dispAndDirection(nanoPosition(:,k),[equilibriumPoint;0;0]);

            nanoForce(:,k) = direction*f_WLCn(tempKelvin,persistenceLengthTag,...
                contourLengthTag,magnitude-nanoRadius,0,100);

            nanoPosition(1,k+1) = overdampedLangevin(nanoPosition(1,k),...
                            nanoBrownian(1,k),nanoForce(1,k),dt,dragCoeffNano);

            nanoPosition(2,k+1) = overdampedLangevin(nanoPosition(2,k),...
                            nanoBrownian(2,k),nanoForce(2,k),dt,dragCoeffNano);

            nanoPosition(3,k+1) = overdampedLangevin(nanoPosition(3,k),...
                            nanoBrownian(3,k),nanoForce(3,k),dt,dragCoeffNano);

            if nanoPosition(3,k+1) < nanoRadius
                nanoPosition(3,k+1) = nanoPosition(3,k+1) + 2*(nanoRadius-nanoPosition(3,k+1));
            end

        end

        for totalPhotonCount = 300000:100000:1500000
            exposureTime = 500E-6; % Choose a specific exposure time for the image generation

            l = round(exposureTime/dt);     % the index of the last positions extracted
            exposedPositionsX = nanoPosition(1,1:l);
            exposedPositionsY = nanoPosition(2,1:l);

            % Generate the specified number of photons for each timestep
            photons = totalPhotonCount/round(exposureTime/dt);
            fullWidthHM = 275 ;     % [nm] Full width half max
            pixelLength = 37.4 ;    % [nm] Length of the pixel
            standardDeviation = fullWidthHM/(2*sqrt(2*log(2))) ;    % [nm] Standard Deviation of
the gaussian approximation of the point spread function
            numberPhotonsDt = poissrnd(photons,1,l);
            photonDistX = standardDeviation*randn(max(numberPhotonsDt),l);
            photonDistY = standardDeviation*randn(max(numberPhotonsDt),l);
            photonX = zeros(max(numberPhotonsDt),l);
            photonY = zeros(max(numberPhotonsDt),l);

            % Distribute the photons to their respective positions
            for k = 1:l
                for m = 1:numberPhotonsDt(k)
                    photonX(m,k) = exposedPositionsX(1,k) + photonDistX(m,k);
                    photonY(m,k) = exposedPositionsY(1,k) + photonDistY(m,k);
                end
            end

            % Convert the photon positions into an image
            image = imageConversion(position2Pixels(photonX,photonY,pixelLength),noiseStandDev);

            % Write image data to a file
```

```
imwrite(image,['W:\FIESTA(source)\bin\TetheredParticle_contLength',num2str(contourLengthTag),...
                'nm_persLength',num2str(persistenceLengthTag),'nm_diameter',...
            (num2str(2*nanoRadius)),'nm_',num2str(exposureTime),'sExpT_',num2str(photons),...
            'PhotonsPerDt_',num2str(pixelLength),'nmPixel_noise',num2str(noiseStandDev),...
            '.tif'],'Compression',...
            'None','WriteMode','append')

        end

    end
end
```

Appendix B - MATLAB function for collision reconciliation

```matlab
function [collisionPosition1,finalPosition1,collisionPosition2,finalPosition2] =
brownianScatteringDifferentDrag(initialPosition1,initialPosition2,...

velocity1,velocity2,collisionTime,timeStep,brownianScatteringMatrix)
% Takes initial positions, fake velocities, and the scattering matrix
% consisting of their diffusion coefficients, and outputs the


    % Bring Objects into contact

    collisionPosition1(1) = initialPosition1(1) + velocity1(1)*collisionTime;
    collisionPosition1(2) = initialPosition1(2) + velocity1(2)*collisionTime;
    collisionPosition1(3) = initialPosition1(3) + velocity1(3)*collisionTime;

    collisionPosition2(1) = initialPosition2(1) + velocity2(1)*collisionTime;
    collisionPosition2(2) = initialPosition2(2) + velocity2(2)*collisionTime;
    collisionPosition2(3) = initialPosition2(3) + velocity2(3)*collisionTime;

    % Find direction between objects
    collisionPosition1 = collisionPosition1';
    collisionPosition2 = collisionPosition2';
    relativePosition = collisionPosition2-collisionPosition1;
    direction = relativePosition/norm(relativePosition);

    % Compute the scattering velocity etc.
    magVelocity1 = velocity1'*direction;
    magVelocity2 = velocity2'*direction;
    newVelocity1 = brownianScatteringMatrix(1,1)*magVelocity1 +
brownianScatteringMatrix(1,2)*magVelocity2;
    newVelocity2 = brownianScatteringMatrix(2,1)*magVelocity1 +
brownianScatteringMatrix(2,2)*magVelocity2;

    % Compute the response velocity
    newVelocity1 = velocity1 - magVelocity1*direction + newVelocity1*direction;
    newVelocity2 = velocity2 - magVelocity2*direction + newVelocity2*direction;

    finalPosition1(1) = collisionPosition1(1) + newVelocity1(1)*(timeStep-
collisionTime);
    finalPosition1(2) = collisionPosition1(2) + newVelocity1(2)*(timeStep-
collisionTime);
    finalPosition1(3) = collisionPosition1(3) + newVelocity1(3)*(timeStep-
collisionTime);

    finalPosition2(1) = collisionPosition2(1) + newVelocity2(1)*(timeStep-
collisionTime);
```

```
    finalPosition2(2) = collisionPosition2(2) + newVelocity2(2)*(timeStep-
collisionTime);
    finalPosition2(3) = collisionPosition2(3) + newVelocity2(3)*(timeStep-
collisionTime);

end
```

BIBLIOGRAPHY

1.   Hirokawa, N., Y. Noda, Y. Tanaka, and S. Niwa. 2009. Kinesin superfamily motor proteins and intracellular transport. Nat. Rev. Mol. Cell Biol. 10: 682–696.

2.   Hancock, W.O. 2014. Bidirectional cargo transport: moving beyond tug of war. Nat. Rev. Mol. Cell Biol. 15: 615–628.

3.   Monroy, B.Y., D.L. Sawyer, B.E. Ackermann, M.M. Borden, T.C. Tan, and K.M. Ori-McKenney. 2018. Competition between microtubule-associated proteins directs motor transport. Nat. Commun. 9: 1487.

4.   Fitzpatrick, A.W.P., B. Falcon, S. He, A.G. Murzin, G. Murshudov, H.J. Garringer, R.A. Crowther, B. Ghetti, M. Goedert, and S.H.W. Scheres. 2017. Cryo-EM structures of tau filaments from Alzheimer's disease. Nature. 547: 185–190.

5.   Vale, R.D., and R.A. Milligan. 2000. The Way Things Move: Looking Under the Hood of Molecular Motor Proteins. Science (80-.). 288: 88–95.

6.   Yildiz, A., M. Tomishige, R.D. Vale, and P.R. Selvin. Kinesin Walks Hand-Over-Hand. : 15–18.

7.   Mickolajczyk, K.J., N.C. Deffenbaugh, J. Ortega Arroyo, J. Andrecka, P. Kukura, and W.O. Hancock. 2015. Kinetics of nucleotide-dependent structural transitions in the kinesin-1 hydrolysis cycle. Proc. Natl. Acad. Sci. 112: E7186–E7193.

8.   Isojima, H., R. Iino, Y. Niitani, H. Noji, and M. Tomishige. 2016. Direct observation of intermediate states during the stepping motion of kinesin-1. Nat. Chem. Biol. 12: 290–

297.

9.   Milic, B., J.O.L. Andreasson, W.O. Hancock, and S.M. Block. 2014. Kinesin processivity

        is gated by phosphate release. Proc. Natl. Acad. Sci. U. S. A. 111: 14136–40.

10.   Selvin, P.R., and T. Ha. 2008. Single-molecule techniques. Cold Spring Harbor

        Laboratory Press.

11.   Yildiz, A., and P.R. Selvin. 2005. Fluorescence imaging with one nanometer accuracy:

        Application to molecular motors. Acc. Chem. Res. 38: 574–582.

12.   Yildiz, A., M. Tomishige, and R.D. Vale. 2004. Kinesin walks hand-over-hand. Science.

        303: 676–678.

13.   Thompson, R.E., D.R. Larson, and W.W. Webb. 2002. Precise Nanometer Localization

        Analysis for Individual Fluorescent Probes. Biophys. J. 82: 2775–2783.

14.   Svoboda, K., and S.M. Block. 1994. Force and velocity measured for single kinesin

        molecules. Cell. 77: 773–84.

15.   Soppina, V., S.R. Norris, A.S. Dizaji, M. Kortus, S. Veatch, M. Peckham, and K.J.

        Verhey. 2014. Dimerization of mammalian kinesin-3 motors results in superprocessive

        motion. Proc. Natl. Acad. Sci. U. S. A. 111: 5562–5567.

16.   Yasuda, R., H. Noji, M. Yoshida, K. Kinosita, and H. Itoh. 2001. Resolution of distinct

        rotational substeps by submillisecond kinetic analysis of F1-ATPase. Nature. 410: 898–

        904.

17.   Andrecka, J., Y. Takagi, K.J. Mickolajczyk, L.G. Lippert, J.R. Sellers, W.O. Hancock,

        Y.E. Goldman, and P. Kukura. 2016. Interferometric Scattering Microscopy for the Study

        of Molecular Motors. 1st ed. Elsevier Inc.

18.   Ortega-Arroyo, J., and P. Kukura. 2012. Interferometric scattering microscopy (iSCAT):

new frontiers in ultrafast and ultrasensitive optical microscopy. Phys. Chem. Chem. Phys. 14: 15625–36.

19.   Kukura, P., H. Ewers, C. Müller, A. Renn, A. Helenius, and V. Sandoghdar. 2009. High-speed nanoscopic tracking of the position and orientation of a single virus. Nat. Methods. 6: 923–7.

20.   Kellermayer, M.S.Z., S.B. Smith, H.L. Granzier, and C. Bustamante. 1997. Folding-Unfolding Transitions in Single Titin Molecules Characterized with Laser Tweezers. Science (80-.). 276: 1112–1116.

21.   Hariharan, V., and W.O. Hancock. 2011. Insights into the Mechanical Properties of the Kinesin Neck Linker Domain from Sequence Analysis and Molecular Dynamics Simulations. 2: 177–189.

22.   Howard, J. 2001. Mechanics of Motor Proteins and the Cytoskeleton. 2nd ed. Sunderland, MA: Sinauer Associates Inc.

23.   Kutys, M.L., J. Fricks, and W.O. Hancock. 2010. Monte carlo analysis of neck linker extension in kinesin molecular motors. PLoS Comput. Biol. 6.

24.   Strating, P. 1999. Brownian dynamics simulation of a hard-sphere suspension. Phys. Rev. E - Stat. Physics, Plasmas, Fluids, Relat. Interdiscip. Top. 59: 2175–2187.

25.   Scala, A. 2012. Brownian Dynamics Simulation of Polydisperse Hard Spheres. : 1–9.

26.   Kural, C., H. Balci, and P.R. Selvin. 2005. Molecular motors one at a time: FIONA to the rescue. J. Phys. Condens. Matter. 17: S3979–S3995.

27.   Ruhnow, F., D. Zwicker, and S. Diez. 2011. Tracking single particles and elongated filaments with nanometer precision. Biophys. J. 100: 2820–2828.

28.   Lee, H., R.M. Venable, A.D. MacKerell, and R.W. Pastor. 2008. Molecular dynamics

studies of polyethylene oxide and polyethylene glycol: Hydrodynamic radius and shape anisotropy. Biophys. J. 95: 1590–1599.

29. Murphy, M.C., I. Rasnik, W. Cheng, T.M. Lohman, and T. Ha. 2004. Probing Single-Stranded DNA Conformational Flexibility Using Fluorescence Spectroscopy. Biophys. J. 86: 2530–2537.

30. ThermoFisher. EZ-Link Maleimide-PEG2-Biotin. .

31. Hwang, W., M.J. Lang, and M. Karplus. 2008. Force Generation in Kinesin Hinges on Cover-Neck Bundle Formation. Structure. 16: 62–71.

32. Shang, Z., K. Zhou, C. Xu, R. Csencsits, J.C. Cochran, and C. V Sindelar. 2014. High-resolution structures of kinesin on microtubules provide a basis for nucleotide-gated force-generation. Elife. 3: 1–27.

33. Goodsell, D.S. 2005. Kinesin. RCSB Protein Data Bank. .

ACADEMIC VITA
Annan S. I. Cook

EDUCATION

THE PENNSYLVANIA STATE UNIVERSITY	University Park, PA

SCHREYER HONORS COLLEGE
Bachelor of Science, Physics
- Medical Option
- Minor and Honors in Biomedical Engineering

RESEARCH/WORK EXPERIENCE

Professor William Hancock Lab, The Pennsylvania State University

Fall 2018 Gained valuable experimental experience with *in vitro* motility assays using motor proteins and fluorescence microscopy techniques.

2017-2018 Designed and implemented computational models of kinesin motor protein dynamics and single molecule, TIR dark-field, gold nanoparticle label microscopy experiments.

Professor James Adair Lab, The Pennsylvania State University

2014-2015 Investigated the physical properties of calcium phosphosilicate nanoparticles for chemotherapeutic drug delivery, localization of radiation therapy agents, and *in vivo* imaging.

PUBLICATIONS

2018 K.J. Mickolajczyk*, **A.S.I. Cook** *, J. Fricks, J. Jethva, and W.O. Hancock, Biophys. J. (2019). (In review, * denotes equal contribution)

PRESENTATIONS

2019 "Insights into kinesin-1 stepping dynamics from Brownian dynamics simulations and high-resolution tracking of gold nanoparticle-labeled motors", Biophysical
2018 Society Annual Meeting, 2019

"Insights into kinesin-1 stepping dynamics from Brownian dynamics simulations and high-resolution tracking of gold nanoparticle-labeled motors", Eberly College of Science Poster Exhibition, 2018

"Using Brownian Dynamics Simulations to Identify Best Practices in Single Particle Tracking", Biophysical Society Annual Meeting, 2018

2017 "Interpreting Motor Protein nanoparticle tracking experiments using Brownian Dynamics simulations" Summer Translational Cardiovascular Institute Research Experience for Undergraduates, 2017

TEACHING

2018 Learning assistant for an upper level mechanics course.
- Provided assistance during guided problem solving activities in class.

- Hel
  d
  office hours once a week to guide learning and assist with homework
  question

ACTIVITIES

2017   Penn State Outing Club
- Conducted hiking and camping trips into the local state parks to introduce inexperienced backpackers to the outdoors.

Penn State Chapter of Society of Physics Students
- Promoted scientific literacy in the local community by presenting physics in local elementary schools.

2016   Animal Rehabilitation and Racing
- Rescued a severely abused donkey from a neglectful environment.
- Trained the donkey to race in order to improve his fitness and mental health for the Fairplay, CO burro race.

HONORS & AWARDS

2018   Lewis C. Cowley Scholarship
J & E Teasdale Science Scholarship
Pre-Eminence in Honors Education Scholarship

2017   Summer Translational Cardiovascular Research Institute REU
Elsbach Honors Scholarship in Physics

2016   Matthew J. Wilson Honors Scholarship

2014   Schreyer Honors Scholar
U.S. Steel Undergraduate Research Fellowship
President's Freshman Award (4.0 GPA)

PROFESSIONAL MEMBERSHIPS

2018   Biophysical Society Student Member

2016   Sigma Pi Sigma Member (National Physics Honor Society